Available online at www.sciencedirect.com
ScienceDirect
Trans. Nonferrous Met. Soc. China 35(2025) 2500−2520
Transactions of Nonferrous Metals Society of China
www.tnmsc.cn

MIG welding microstructure, residual stress and mechanical properties of powder metallurgy 7A52 aluminum alloys

Jing-han YANG[1,2,3], Peng-fei JI[4], Lin-yang WU[1,2,3], Xiao-yun DING[1,2,3], Jin-chao JIAO[1,2,3], Meng-hui CUI[1,2,3], Xing-yu CHEN[1,2,3], Jin ZHANG[1,2,3], Yong LIAN[1,2,3], Lin ZHENG[5], Shi-tao DOU[1,5]

1. Institute for Advanced Materials and Technology, University of Science and Technology Beijing, Beijing 100083, China;
2. Beijing Key Laboratory of Corrosion, Erosion and Surface Technology, University of Science and Technology Beijing, Beijing 100083, China;
3. National Materials Corrosion and Protection Data Center, University of Science and Technology Beijing, Beijing 100083, China;
4. Institute of Engineering Technology, University of Science and Technology Beijing, Beijing 100083, China;
5. Southwest Technology and Engineering Research Institute, Chongqing 400039, China

Received 26 June 2024; accepted 13 February 2025

Abstract: The MIG welding of in-situ generated nano-Al_2O_3 powder metallurgy 7A52 (PM 7A52) aluminum alloy was investigated. The microstructure was characterized using EBSD and TEM, while macrotexture and internal residual stresses were analyzed with a self-developed SWXRD technique. The results revealed that PM 7A52 aluminum alloy effectively reduced the grain size, dislocation density, and texture strength in the post-weld microstructure. Furthermore, the residual stress in the weld zone (WZ) of PM 7A52 aluminum alloy was reduced by 38 MPa compared to that of the conventional melt-cast 7A52 (CM 7A52) aluminum alloy. Notably, the tensile strength and elongation of welded joints in PM 7A52 aluminum alloy were increased by approximately 15% and 26%, respectively. The improvement in joint tensile strength was primarily attributed to grain boundary strengthening and dispersion strengthening caused by γ-Al_2O_3 particles entering the WZ.

Key words: powder metallurgy 7A52 aluminum alloy; MIG welding; SWXRD technique; texture; residual stress; mechanical properties

1 Introduction

The 7xxx series aluminum alloys are extensively used in aerospace, transportation and military armor due to their high specific strength, favorable corrosion resistance and fracture toughness [1−3]. In particular, 7A52 aluminum alloy is widely used in lightly armored vehicle bodies for its high strength, toughness and corrosion resistance [4,5]. MIG welding, known for its low cost, high efficiency, and established technology, has found widespread application across various industries [6−8]. However, conventional melt-cast 7A52 aluminum alloys are prone to grain growth in the weld and heat-affected zone due to the effect of welding heat input, which results in reduced joint strength. Additionally, the large temperature gradients in the weld pool, combined with thermal cycling and microstructural non-uniformity, lead to high residual stresses and uneven distribution within the welded joints, which

Corresponding author: Jin ZHANG, E-mail: zhangjin@ustb.edu.cn; Yong LIAN, Tel: +86-10-82377393, E-mail: liany09@126.com
https://doi.org/10.1016/S1003-6326(25)66829-4

may cause the deformation or cracking of the welded components [9,10].

Several methods are available to enhance the strength of aluminum alloy base materials and welded joints. For base materials, these methods primarily involve optimizing the ratio of alloying elements [11−13], employing intense plastic deformation techniques such as hydrostatic extrusion [14], and modulating heat treatment processes to control precipitation behavior [15,16]. To improve the strength of welded joints, researchers have focused on strategies such as adding trace elements [17−19], using alternative filler materials [20,21], optimizing welding parameters [22,23], employing different welding methods [24], and incorporating auxiliary techniques like ultrasound and magnetic fields [25,26]. In recent years, introducing ceramic particles, such as TiB_2, SiC, TiC, and B_4C, has shown promise in improving the mechanical properties of welded joints [27,28]. However, achieving a uniform distribution of externally added ceramic particles remains challenging. Larger particle sizes often result in insufficient weld strengthening [29], while excessive additions may cause particle aggregation and weaken bonding with the matrix [30]. Thus, not all secondary phase particles are beneficial to enhancing joint performance [31]. Powder metallurgy aluminum alloys, as a new class of lightweight structural materials, have gained widespread application in aerospace, military, and automotive fields [32,33]. These materials can suppress grain boundary migration caused by welding heat input and limit grain growth in the heat-affected zone [34,35]. The in-situ generation of Al_2O_3 ceramic particles offers dispersion strengthening, which can induce lattice distortion and texture evolution, potentially influencing the distribution and formation of residual stresses in the weld region.

Several studies have investigated residual stresses in welded joints. For example, SABRY et al [36] used neutron diffraction to examine the stresses in stir friction welds of 6061 and A365 dissimilar aluminum alloys, revealing that welding sequences in multi-pass processes can influence the residual stresses. In another study, synchrotron radiation techniques were employed to test the residual stresses in the MIG butt weld microstructure of 8 mm-thick 5083 aluminum plates, where transverse tensile residual stresses of up to 55 MPa were detected in the weld zone after fatigue cycling [37]. Non-destructive methods for measuring internal residual stresses include high-energy X-ray diffraction, neutron diffraction, and ultrasonic techniques [38,39]. However, ultrasonic methods face limitations in performing spot tests for residual stresses in different areas of welded joints. Additionally, neutron diffraction and high-energy synchrotron radiation require large, specialized equipment and limited machine time, restricting their use for long-term weld stress studies. Consequently, accurate measurement and control of residual stresses within welded joints is crucial. To address this, we have independently developed short-wavelength X-ray diffraction (SWXRD) technology. This technique enables non-destructive, full-area, fixed-point, and high-precision residual stress measurement by adjusting the diffraction volume position within the weld seam [40,41].

MIG welding of 7xxx aluminum alloys is widely applied; however, challenges such as suboptimal microstructure, relatively low strength in welded joints, and high residual stress remain prevalent. This study introduces an innovative approach to enhance the microstructure and mechanical properties of powder metallurgy (PM) 7A52 aluminum alloy by in-situ generation of Al_2O_3 nanoparticles. Additionally, the residual stress within the welded joints was characterized using the self-developed SWXRD technique. The primary goal of this research was to achieve high-performance, low-anisotropy welded microstructures in powder metallurgy aluminum alloys. These improvements are significant for advancing the application of 7A52 aluminum alloy MIG welding in aerospace, transportation, and military armor.

2 Experimental

2.1 Materials and welding method

The production process for in-situ generated nano-Al_2O_3 dispersion strengthening PM 7A52 aluminum alloy was as follows. Commercial aluminum, Al−50Zn alloy, magnesium, and copper powders were used as raw materials. The raw materials were then mixed and ball-milled using a

V-mixer and a drum ball mill, respectively. Next, the mixture was compacted in a cold isostatic press at 180 MPa for 3 min. Following compaction, the blanks were vacuum sintered at 580 °C for 2 h to obtain aluminum alloy ingots. Hot extrusion was subsequently performed at 420 °C with an extrusion speed of 0.3 mm/s and an extrusion ratio of 4:1. The width and thickness of the extruded plate were 150 mm and 13.5 mm, respectively. Finally, T6 heat treatment was conducted, consisting of solution treatment at 470 °C for 2 h followed by artificial aging at 120 °C for 24 h. A schematic diagram of the PM 7A52 aluminum alloy plate preparation process is shown in Fig. 1. For comparative analysis, the extrusion ratio and heat treatment process of CM 7A52 aluminum alloy were kept the same as those for PM 7A52. The elemental composition of 7A52 aluminum alloy is provided in Table 1.

The metal inert gas (MIG) welding process was employed to join two plates along the transverse direction, with the welding schematic shown in Fig. 2(a). The welding wire used was ER 5356, with a diameter of 1.2 mm, and its elemental composition is provided in Table 1. The welding operation was carried out using a KEMPPI KempArc Pulse 450 system, and the dimensions of the welded samples were 150 mm × 90 mm × 13.5 mm. The welding parameters are detailed in Table 2. Double-sided welding was performed, with five layers welded on the front side. The first two layers were welded in one pass, while the last three layers required three passes. The back side was welded with a single layer and one pass. The welding parameters remained consistent for each pass, and the welded samples were left for 1 d before proceeding with subsequent experiments.

2.2 Morphology and microstructure characterization

The metallurgical microstructure of the base metal (BM), heat-affected zone (HAZ) and weld zone (WZ) was observed using an optical microscope (ZEISS, Axioskop.A1, German). A scanning electron microscope (ZEISS, Sigma 500, German) equipped with the energy dispersive spectroscopy (EDS) detector was used to characterize the phases and elemental distribution of the weld microstructure.

Electron backscatter diffraction (EBSD) tests were conducted using a field emission scanning electron microscope (ZEISS, SUPRATM 55, Germany) with an EBSD probe. Al_2O_3 particles and dislocation distribution characteristics were analyzed using a transmission electron microscope (Tecnai G2 F30, FEI, USA).

The physical analysis of the welded microstructure was performed using an X-ray diffractometer (Rigaku, Ultima IV, Japan) with Cu K_α radiation.

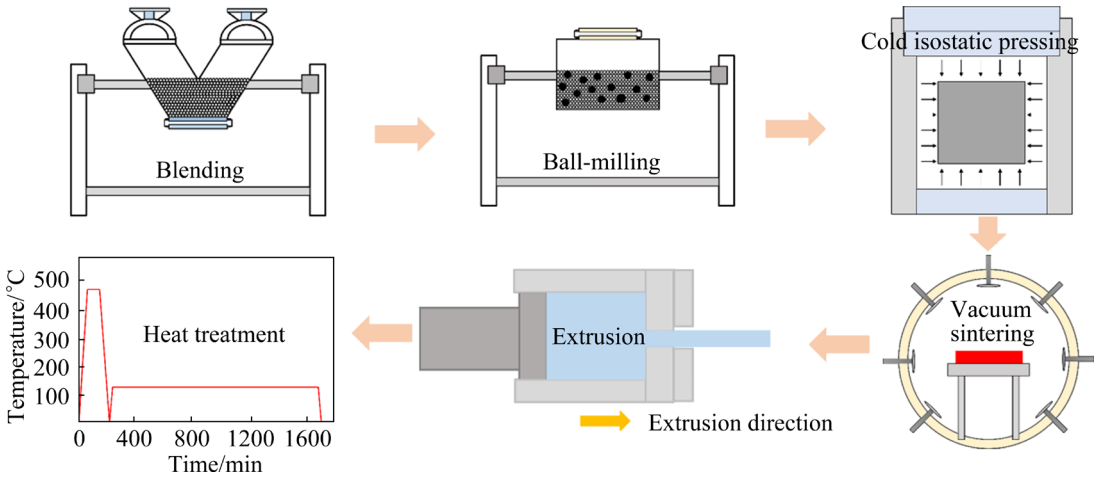

Fig. 1 Schematic diagram of preparation process for PM 7A52 aluminum alloy plate

Table 1 Compositions of 7A52 base metal and ER 5356 welding wire (wt.%)

Sample	Si	Fe	Cu	Mn	Mg	Cr	Zn	Ti	Zr	Al
7A52	0.25	0.30	0.05−0.20	0.20−0.50	2.00−2.80	0.15−0.25	4.00−4.80	0.05−0.18	0.15	Bal.
ER 5356	0.25	0.40	0.10	0.05−0.20	4.50	5.50	0.05	0.20	0.10	Bal.

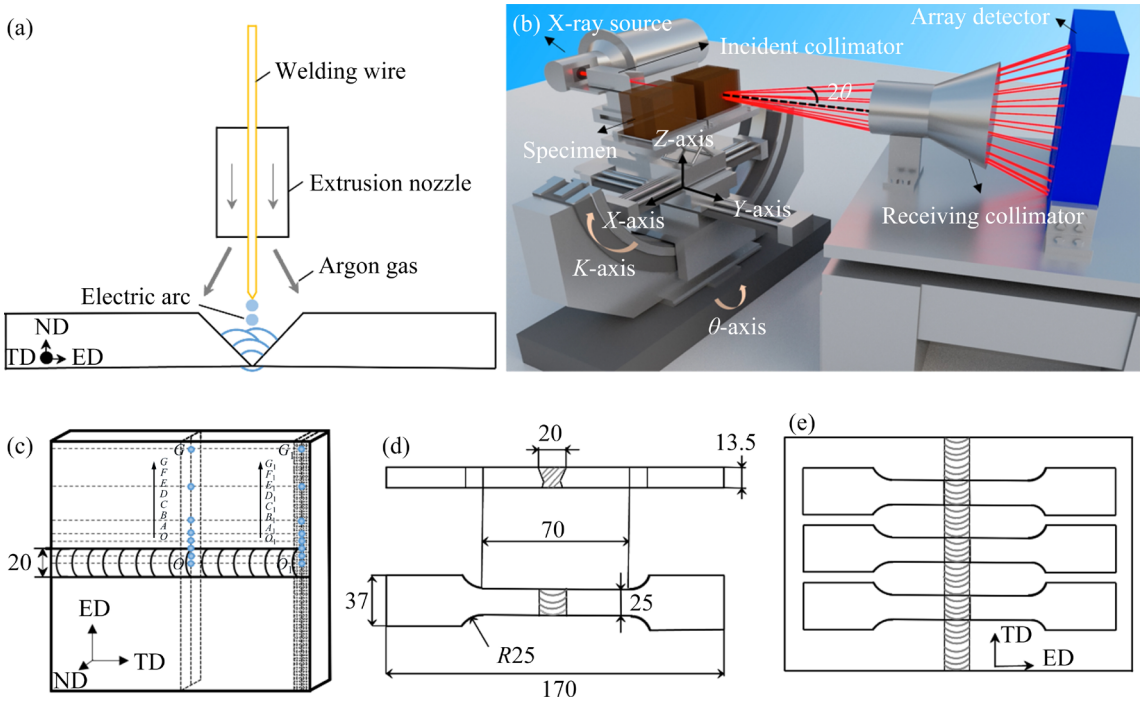

Fig. 2 Schematic diagrams of MIG welding (a), SWXRD test (b), distribution of test point locations (c), tensile specimen dimension (d), and sampling location (e) (unit: mm)

Table 2 Welding process parameters

Angle of welding torch/(°)	Shielding gas	Welding speed/ (m·min^{-1})	Wire feed rate/ (m·min^{-1})	MIG current/A	MIG voltage/V	Shielding gas flow rate/ (L·min^{-1})	Swing parameter/ mm
60	Pure argon	0.15	18	230	25	30	2.5

The scanning angle range was 10°−120°, and the scanning speed was 1 (°)/min. Macrotexture testing was carried out using a self-developed short-wavelength X-ray diffractometer (SWXRD−2000, China), equipped with a tungsten target. The operating voltage and current were set to 200 kV and 4 mA (λ=0.208992 Å), with the (111) crystal plane and a diffraction angle of 5.123°. Parallel X-rays were directed into the crystal, generating diffraction lines that were received by a collimator, satisfying the Bragg equation. The final exposure was captured on an array detector, revealing the Debye ring. A schematic diagram of the equipment is shown in Fig. 2(b).

2.3 Residual stress and mechanical properties test

Both internal residual stress and macrotexture tests were performed using the SWXRD instrument. The residual stress measurement followed the principle of neutron diffraction [42] and was obtained by the method based on Bragg's law, as outlined in Eqs. (1) and (2). Stress-free specimens were prepared by cutting the material into a grid with a size of 5 mm × 5 mm and a depth of 10 mm to release residual stress. Residual stresses in the extruded direction (ED) and transverse direction (TD) of the welded plate were calculated under the assumption of planar stress, as shown in Eqs. (3) and (4). The test depth was for the central layer of the plate.

$$2d_{hkl}\sin\theta=\lambda \tag{1}$$

$$\varepsilon=\left(d_{hkl}-d_0\right)/d_0 \tag{2}$$

$$\sigma_{xx}=E_{hkl}/\left(1-v_{hkl}^2\right)\left(\varepsilon_{xx}+v_{hkl}\varepsilon_{yy}\right) \tag{3}$$

$$\sigma_{yy}=E_{hkl}/\left(1-v_{hkl}^2\right)\left(\varepsilon_{yy}+v_{hkl}\varepsilon_{xx}\right) \tag{4}$$

where d_{hkl} and d_0 represent the lattice spacings of the welded specimen and stress-free specimen with (hkl) crystal plane, respectively. θ is the diffraction angle and λ is the wavelength. ε and σ are the strain

and residual stress, respectively. E_{hkl} and v_{hkl} denote Young's modulus and Poisson's ratio, respectively. The distribution of residual stress test points, perpendicular to the welding direction, is shown in Fig. 2(c) and Table 3. Points O−G represent the actual test locations for residual stress, while points O_1−G_1 correspond to the test locations for stress-free specimens.

Table 3 Distribution of test points for internal residual stress in MIG welding

Test point	Distance to welding center/mm	Region
O, O_1	0	WZ
A, A_1	5	
B, B_1	10	HAZ
C, C_1	15	
D, D_1	20	
E, E_1	30	BM
F, F_1	60	
G, G_1	90	

The microhardness perpendicular to the weld direction was measured using an HXD−1000TMC/LCD microhardness tester. A loading force of 1.96 N and a dwell time of 15 s were applied. Tensile testing of the welds was conducted using the MTS Landmark tester at room temperature, with a strain rate of 0.5 mm/min. The dimensions of the dog-bone tensile specimens were 37 mm in width, 13.5 mm in thickness, and 170 mm in total length, as shown in Fig. 2(d). Three tensile specimens were selected as parallel samples. The tensile strength and elongation were calculated by averaging the measurements, and one set of data was used to construct the stress−strain curve. The sampling location is shown in Fig. 2(e).

3 Results

3.1 Morphology

The metallographic microstructure of BM and WZ for PM 7A52 and CM 7A52 aluminum alloys are shown in Figs. 3(a1)−(d1). The BM of both materials exhibited a typical rolling microstructure, with the grain size perpendicular to the ND being larger than that in the other two directions. PM 7A52 displayed a noticeable reduction in grain size along all three directions compared to CM 7A52. A comparison of the WZ microstructures (Figs. 3(c1) and (d1)) reveals that the grains in all three directions exhibited an equiaxed structure in both materials.

To further investigate potential differences in the phases of the two materials, the microstructure was analyzed in greater detail (as shown in Figs. 3(a2)−(d2) and (a3)−(d3)). Local face-scanning elemental analysis of the BM in Areas 2 and 4 revealed that its elemental composition was consistent with that of the 7A52 aluminum alloy (as shown in Table 1). The WZ exhibited higher levels of Mg_2Si and $MgZn_2$ phases due to the relatively high magnesium content in the ER 5356 wire, along with the presence of some Al_2Cu phases. Notably, the size and distribution of the phases were similar in both PM 7A52 and CM 7A52 welds. Elemental distribution scanning results of the WZ also revealed that the Zn content was higher than that of the standard ER 5356, while the Cr content was lower. This variation may be attributed to some of the BM material entering the WZ in a molten state, which solidified during welding and caused changes in elemental composition.

3.2 Macrotexture

To further investigate the composition and content of the phases, XRD analyses were conducted on both the BM and WZ (Figs. 4(a) and (b)). The phase compositions in the BM and WZ of the PM 7A52 and CM 7A52 aluminum alloys were found to include Al, Mg_2Si, Al_2Cu, and $MgZn_2$. Notably, the peak strengths of these phases in the BM and WZ of PM 7A52 were comparable to those of CM 7A52. However, the strongest peak intensities in the BM and WZ of PM 7A52 were lower than those of CM 7A52, which may be attributed to differences in texture. As shown in Figs. 4(c)−(f), the diffraction Debye rings for the (111) plane in the BM and WZ are depicted, with colors ranging from blue to red representing intensity from low to high. It is evident that the diffraction intensity at characteristic points of the Debye rings in the BM and WZ of PM 7A52 was lower than that in CM 7A52. Furthermore, the diffraction intensity distribution curves around the Debye rings (Figs. 4(g) and (h)) indicate that the fluctuation range of diffraction intensity in the BM and WZ of PM 7A52 was narrower compared to that of CM 7A52.

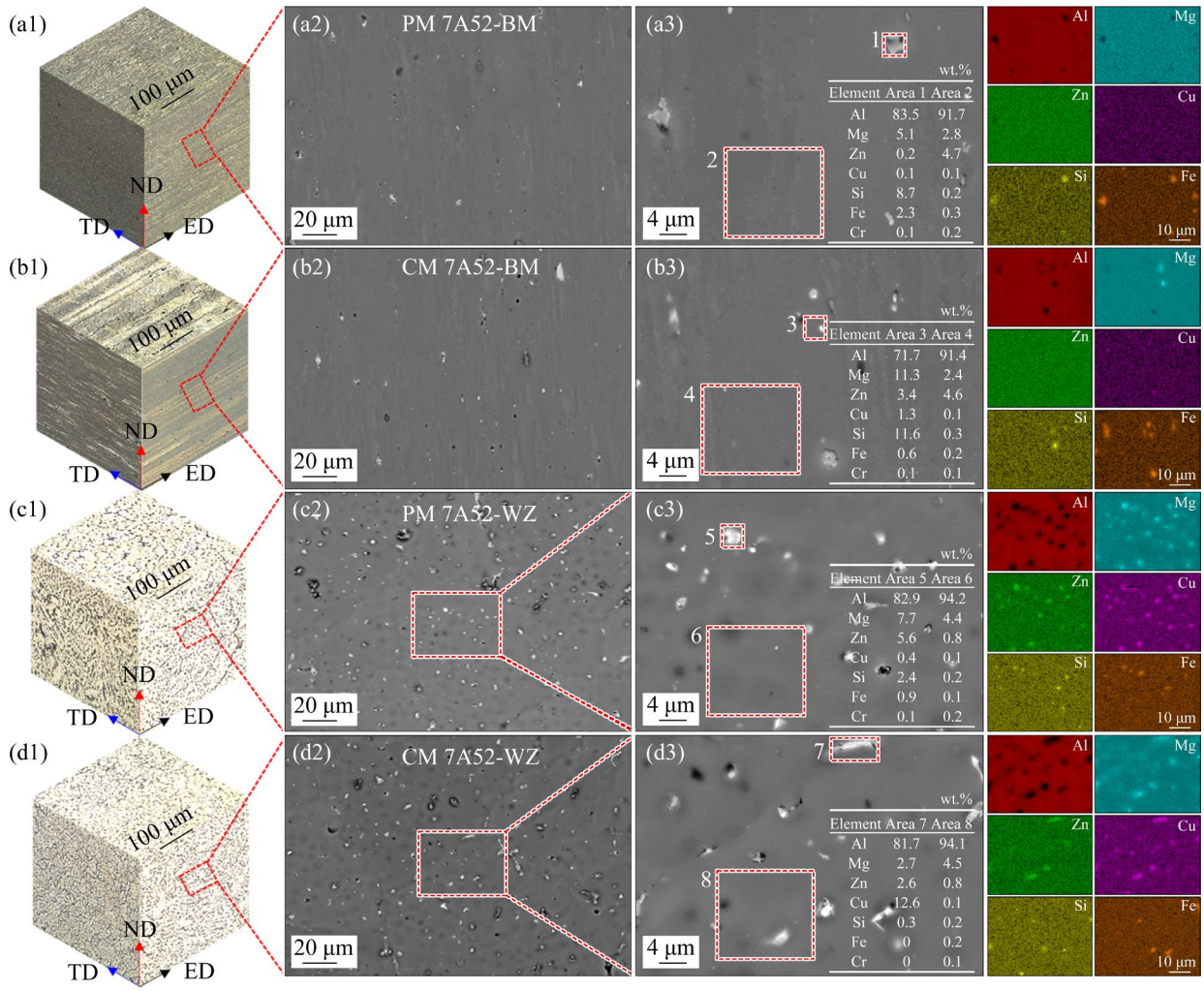

Fig. 3 3D metallographic microstructure (a1−d1), SEM microstructure (a2−d2), and EDS elemental scanning results (a3−d3) of BM for PM 7A52 (a1−a3) and CM 7A52 (b1−b3), as well as WZ for PM 7A52 (c1−c3) and CM 7A52 (d1−d3)

3.3 Microstructure

3.3.1 Grain size

The microstructural transformation during the welding process significantly affected the residual stress and mechanical properties of the welded joints. The grain orientation distributions for the WZ, HAZ, and BM of both materials are shown in Fig. 5. EBSD measurements of the WZ, HAZ, and BM were taken from the center layer of the plate, with the WZ observations focused at the center along the ED. In the BM, the grain color distribution of PM 7A52 aluminum alloy was more uniform compared to CM 7A52, indicating that powder metallurgy aluminum alloys exhibited lower texture (Figs. 5(c) and (i)). Additionally, the grain size of PM 7A52 (5.9 μm) was significantly smaller than that of CM 7A52 (15.4 μm).

The grains in the HAZ were influenced by the weld-heat cycle, resulting in growth compared to the BM while retaining their elongated shape. The grain size in the HAZ of PM 7A52 aluminum alloy (6.8 μm) was significantly smaller than that of CM 7A52 (20.5 μm). In the WZ, most equiaxed grains in PM 7A52 exhibited a random orientation distribution. Additionally, the grains in PM 7A52 were refined, with their size reduced compared to those in CM 7A52.

3.3.2 Grain boundary and dislocation density

The grain boundary size and dislocation density significantly influenced the strength of the weld. The grain boundary size distributions in the WZ, HAZ, and BM are shown in Fig. 6. The number of small-angle grain boundaries in PM 7A52 was higher than that in CM 7A52 for both the BM and WZ. In particular, the proportion of small-angle grain boundaries in the WZ was 14.8%

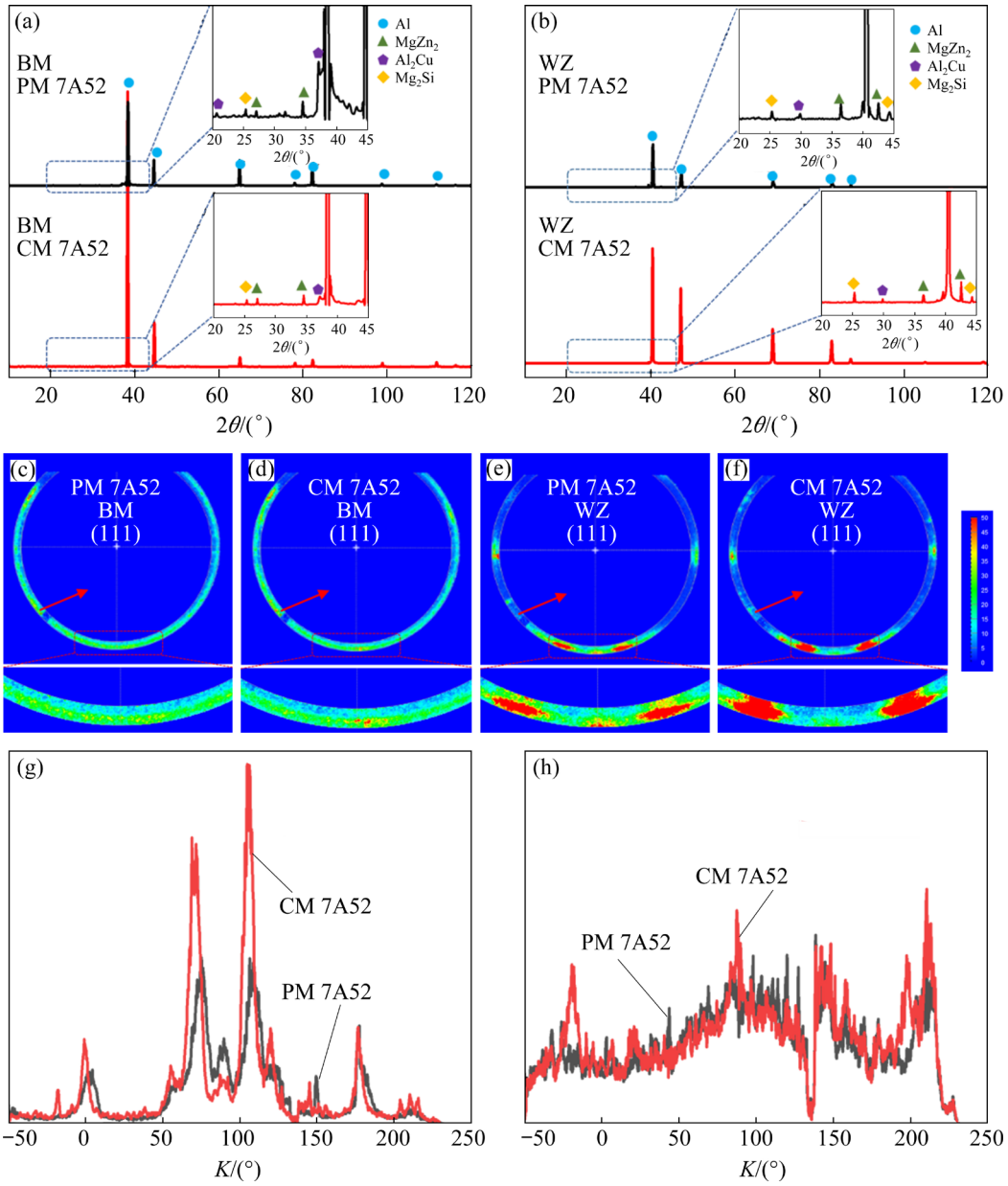

Fig. 4 XRD patterns of BM (a) and WZ (b); Diffraction Debye rings of BM in PM 7A52 (c) and CM 7A52 (d), and WZ in PM 7A52 (e) and CM 7A52 (f) analyzed using SWXRD; Diffraction peak intensity variation curves for BM (g) and WZ (h) (K is the angle along Debye ring)

for PM 7A52 and 9.5% for CM 7A52. This increase of 5.3% in small-angle grain boundaries had a notable impact on the strength of the welded joints.

The local misorientation distribution is shown in Fig. 7. Using Eq. (5) [43], the geometric necessary dislocation density (ρ_{GND}) was calculated based on the average local misorientation (θ_{KAM}). The calculated geometric necessary dislocation density values are provided in Table 4. The results show that the dislocation density of PM 7A52 in the WZ, HAZ, and BM decreased to various degrees compared to that of CM 7A52. Additionally, in the WZ of CM 7A52, regions with higher dislocation density were concentrated, potentially leading to stress concentration and increasing the risk of fracture susceptibility [44].

$$\rho_{GND} \cong 2\theta_{KAM}/(bd) \quad (5)$$

where d is the EBSD scan step, and b is the magnitude of Burger vector for aluminum metal (0.286 nm).

3.3.3 Recrystallization and microtexture

The recrystallization microstructures in the WZ, HAZ, and BM of PM 7252 and CM 7A52 are shown in Figs. 8(a)−(f). In the BM, the CM 7A52

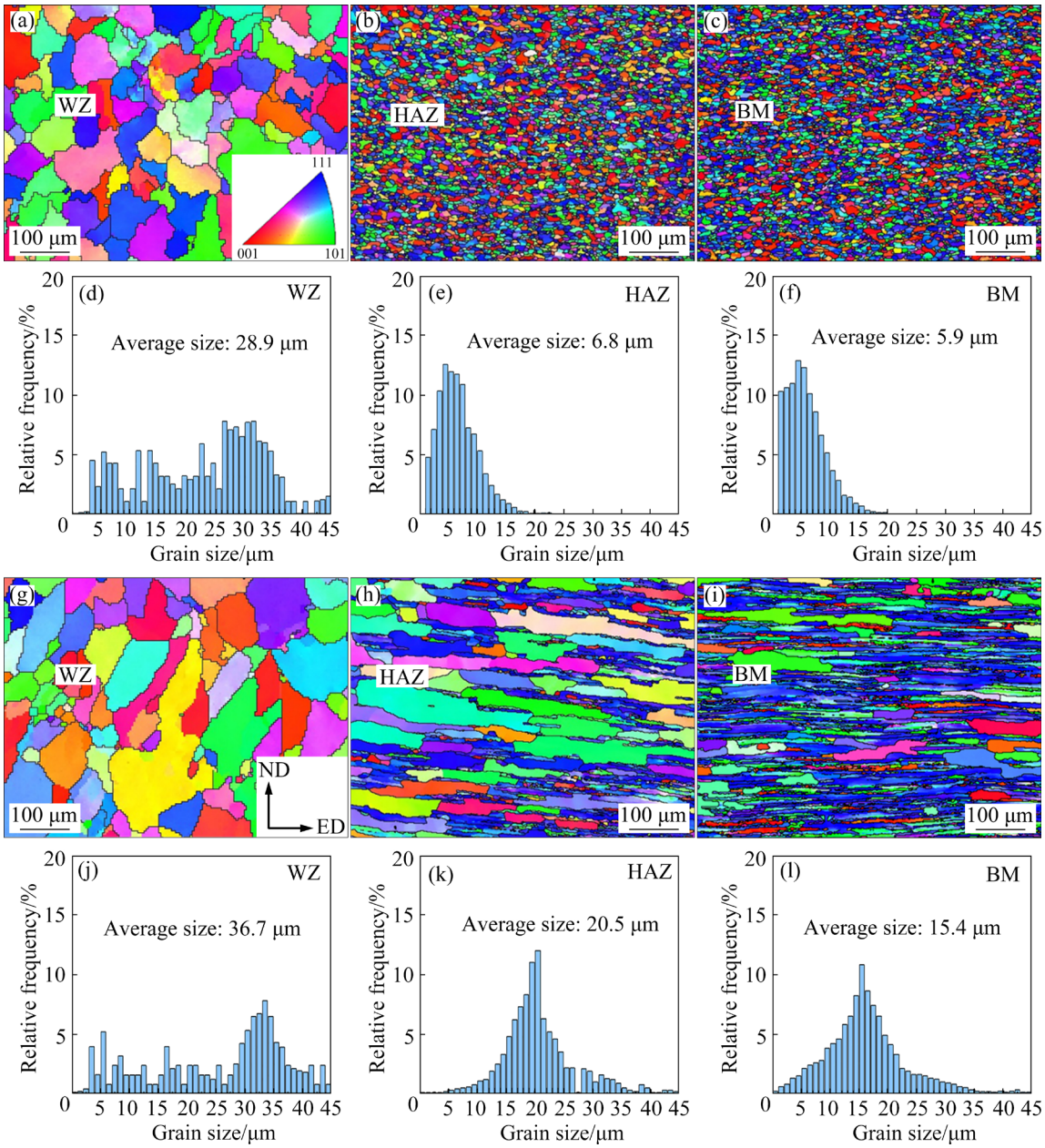

Fig. 5 Grain orientation (a−c, g−i) and grain size distribution (d−f, j−l) in different weld areas of PM 7A52 (a−f) and CM 7A52 (g−l)

exhibited a higher proportion of deformed microstructure, approximately 24.7%. Compared to CM 7A52, the PM 7A52 showed a 17.0% reduction in recovery microstructure and a 21.5% increase in recrystallization microstructure. Welding heat input caused significant changes in the microstructures of the HAZ and WZ as well. In the WZ, the recovery microstructure of PM 7A52 decreased by 21.1%, while its recrystallization microstructure increased by 37.2%.

Figures 8(g)−(l) present the pole figures of the (111) plane for different welding regions. The pole density value of PM 7A52 was consistently lower than that of CM 7A52 across all regions. This finding indicates that the powder metallurgy aluminum alloy exhibited a weaker texture after welding. The weaker texture is attributed to the presence of Al_2O_3 particles, which inhibited dynamic recovery and recrystallization during the deformation, as well as static recovery and recrystallization during heat treatment, resulting in a finer texture structure [45]. Specifically, the pole density values in the BM region were 7.1 for PM 7A52 and 10.7 for CM 7A52. In the WZ, these values were 3.6 and 5.6, respectively.

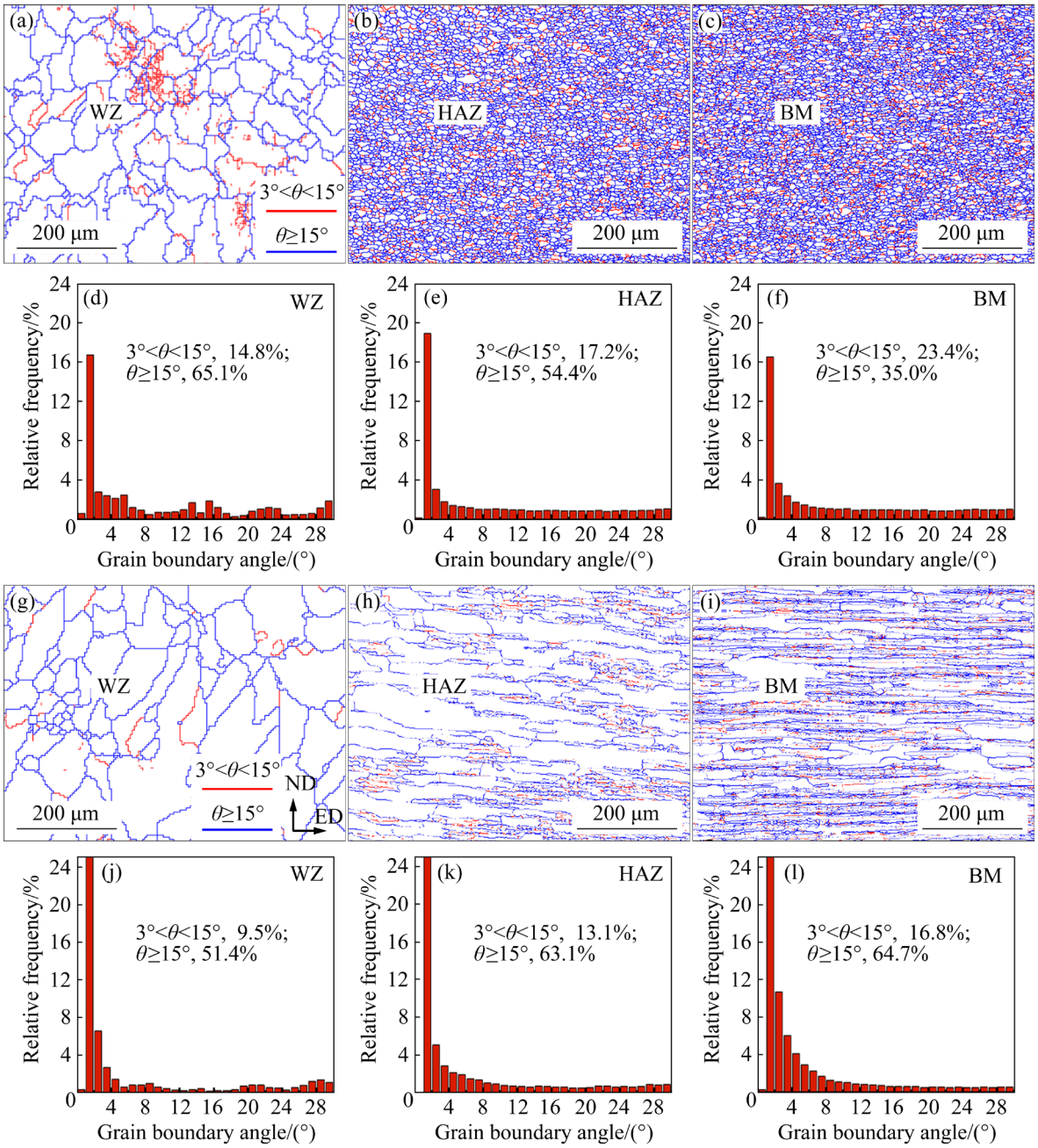

Fig. 6 Grain boundary (a−c, g−i) and grain boundary angle distribution (d−f, j−l) in different weld areas of PM 7A52 (a−f) and CM 7A52 (g−l)

3.4 Residual stress and lattice spacing

Residual stress can significantly influence the mechanical properties, corrosion resistance, and fatigue performance of welded joints. Consequently, measuring and mitigating residual stress in welded joints has been a key research focus. Figures 9(a), (b), (d) and (e) illustrate the lattice spacings of both the welded specimen and the stress-free specimen along the TD and ED for the PM 7A52 and CM 7A52.

In the WZ, the difference in lattice spacing between the welded specimen and the stress-free specimen was smaller for PM 7A52 compared to CM 7A52. This observation is attributed not only to residual stress but also to differences in alloy composition and microstructure. Figures 9(c) and (f) illustrate the internal residual stress distribution curves for PM 7A52 and CM 7A52, respectively. It can be observed that residual stress in the WZ was generally higher than that in the HAZ and the BM. Furthermore, the average peak residual stress in the WZ of CM 7A52 was approximately 38 MPa higher than that of PM 7A52.

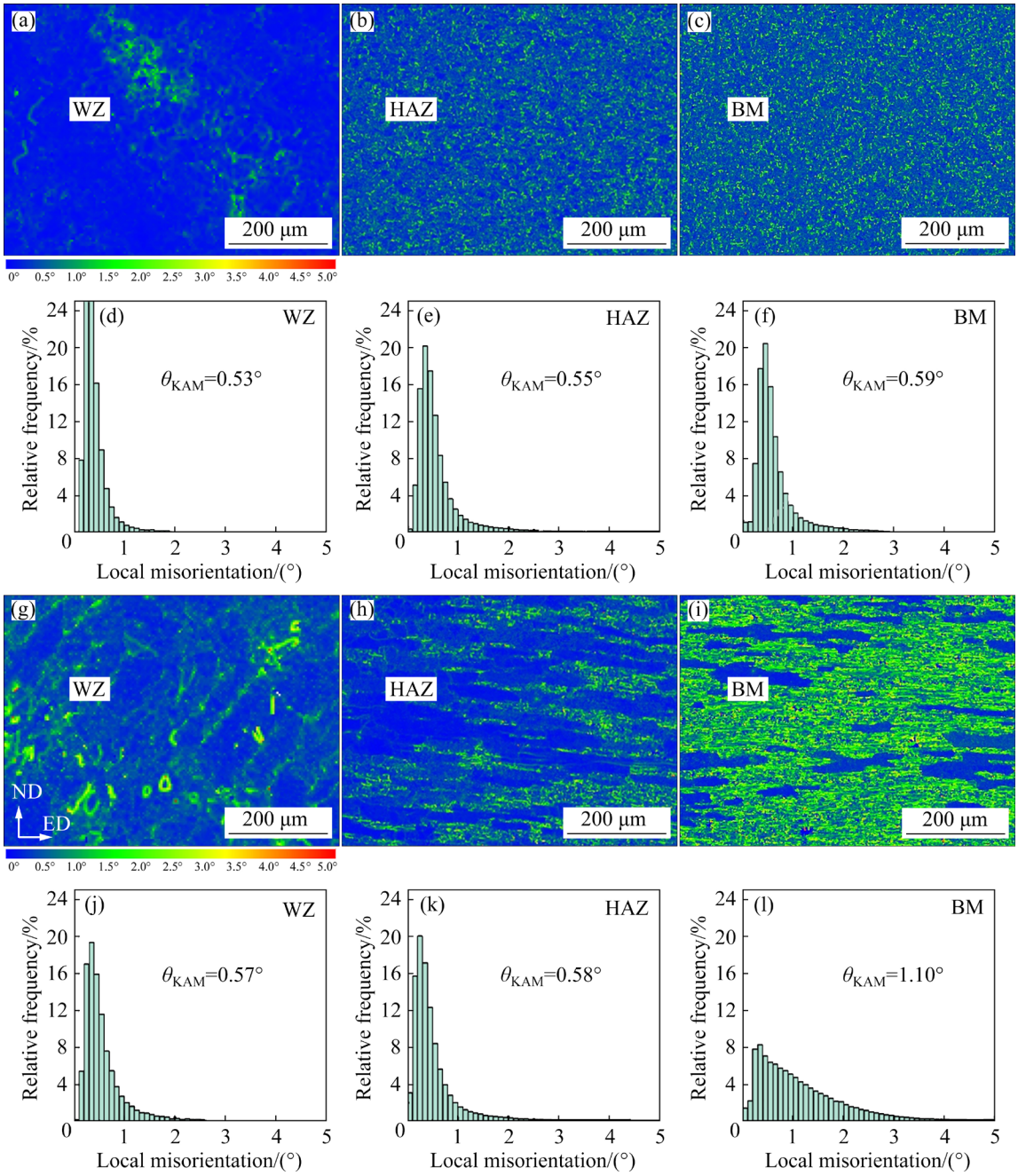

Fig. 7 Local misorientation distribution in different weld areas of PM 7A52 (a−f) and CM 7A52 (g−l)

Table 4 Geometric necessary dislocation density ρ_{GND} in different weld areas

Alloy	$\rho_{GND}/10^{14}$ m^{-2}		
	WZ	HAZ	BM
PM 7A52	1.88	1.95	2.09
CM 7A52	2.03	2.06	3.90

3.5 Mechanical properties

Mechanical properties, such as microhardness and tensile strength, are critical for ensuring the service safety of aluminum alloy weldments. Figures 10(a) and (b) show the microhardness distribution curves from the WZ to the BM. Due to the uneven heat distribution during the welding process, the microhardness profile exhibited a double “W” pattern [46]. Compared to CM 7A52, PM 7A52 demonstrated the improved microhardness in the WZ, HAZ, and BM. Specifically, the microhardness in the BM of PM 7A52 was approximately HV 123, an increase of 20% over CM 7A52 (HV 102). Moving from the BM to the HAZ, the microhardness gradually decreased due to recrystallization in the HAZ, which weakened the

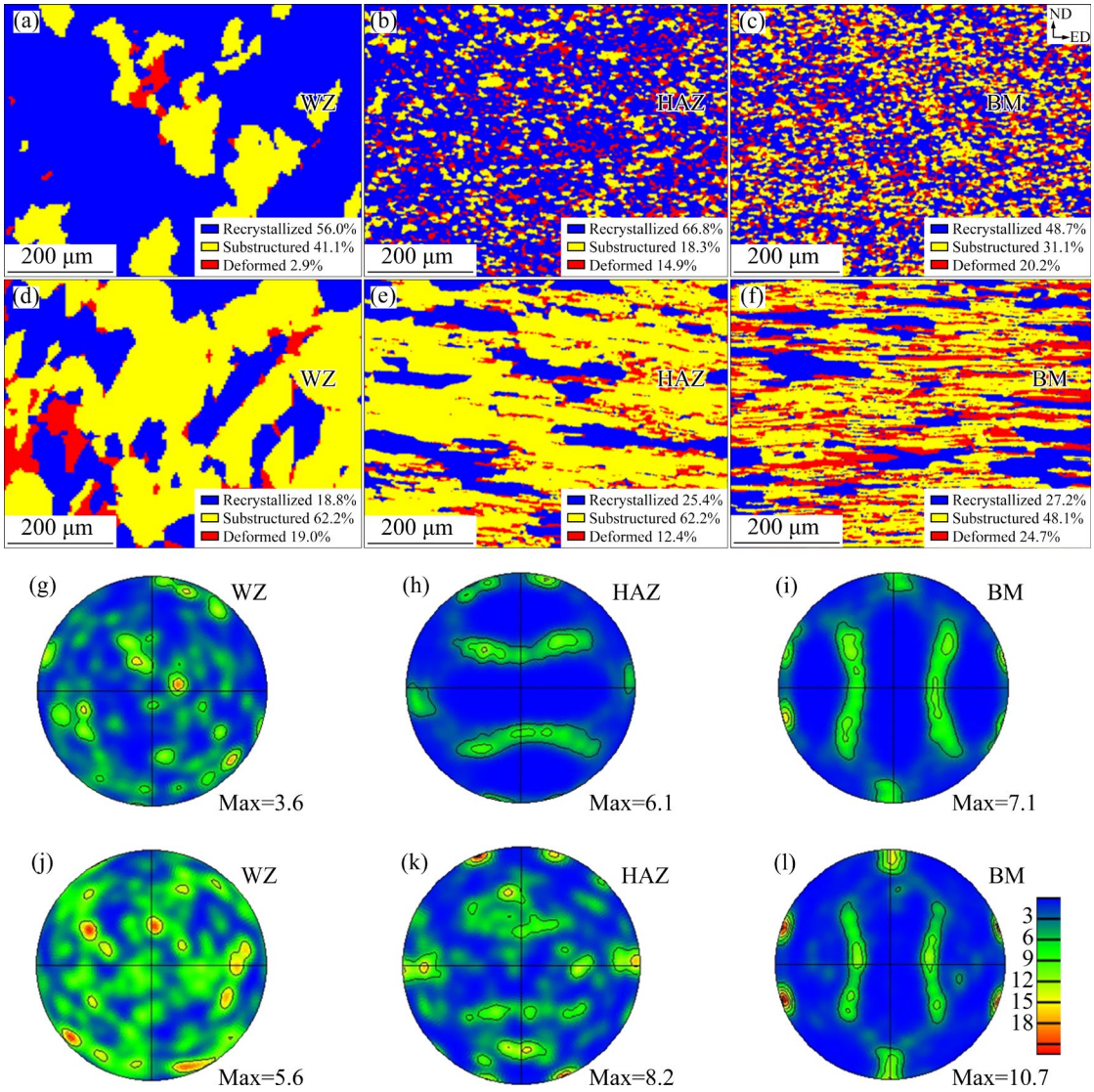

Fig. 8 Recrystallization microstructure distribution in different weld areas of PM 7A52 (a−c) and CM 7A52 (d−f); Pole figures in different weld areas of PM 7A52 (g−i) and CM 7A52 (j−l)

work-hardening effect, and the reduction of strengthening phases in the BM after solution treatment. In the WZ, PM 7A52 exhibited an average microhardness of HV 88, approximately 17% higher than that of CM 7A52 (HV 75). This improvement is likely due to dispersed Al_2O_3 particles in PM 7A52, which entered the molten pool during welding process and refined the weld microstructure, thereby enhancing microhardness (see Figs. 5(a) and (g)).

Figures 10(c) and (d) display the engineering stress−strain curves, and histogram of tensile strength and elongation, respectively. For PM 7A52, the tensile strength and elongation reached 291.3 MPa and 7.3%, respectively, approximately 15% and 26% higher than those of CM 7A52. The tensile fracture morphology, shown in Figs. 10(e)−(j), reveals a denser ligamentous dimple microstructure in PM 7A52 compared to CM 7A52. Despite this, porosity defects were observed in the WZ of both materials due to variations in hydrogen solubility in the aluminum alloy liquid and the supersaturation of hydrogen, which precipitated from the weld and formed porosity. Notably, the addition of Al_2O_3 particles did not increase the porosity in the WZ. The maximum pore diameters in PM 7A52 and CM 7A52 were approximately 0.65 and 0.93 mm, respectively, as shown in Figs. 10(e) and (h). These porosity defects significantly affect the mechanical properties of the materials, highlighting the need to reduce WZ porosity in PM 7A52. The product of strength and

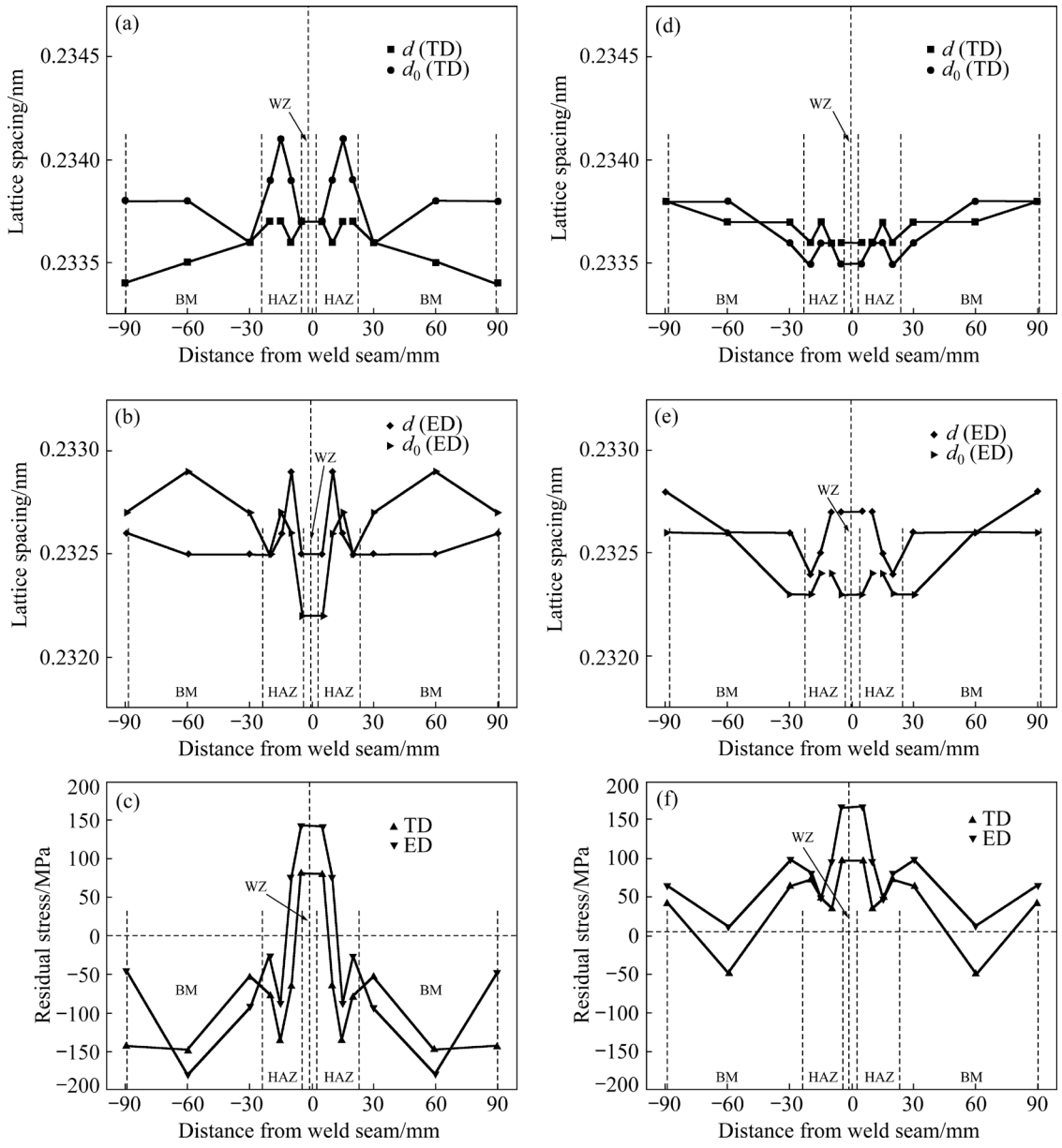

Fig. 9 Lattice spacings of welded specimens and stress-free specimens along TD (a, d) and ED (b, e) in PM 7A52 (a, b) and CM 7A52 (d, e); Internal residual stress along direction perpendicular to weld seam in PM 7A52 (c) and CM 7A52 (f)

elongation, which reflects the material's balance between strength and plasticity [47], was 2.1 GPa·% for PM 7A52, higher than that of CM 7A52 (see Fig. 10(k)).

To further explore the location and mode of tensile fracture, the microstructure near the fracture was examined (Figs. 11(a) and (b)). The results indicate that the fracture in both aluminum alloy materials primarily occurred in the WZ and was predominantly characterized by the transcrystalline fracture. Figures 11(c)−(h) present the distribution of grain boundaries, local misorientation, and Schmid factor near the fracture. A higher number of small-angle grain boundaries near the fracture in PM 7A52 were observed, correlating with its higher tensile strength. Conversely, CM 7A52 exhibited larger local misorientation near the fracture, indicating greater susceptibility to cracking under tensile forces. The Schmid factor, which represents the ratio of shear stress to principal stress after orthogonal decomposition [48], was also higher in CM 7A52. This larger Schmid factor made cracks more prone to initiation and propagation in CM 7A52 [49−51].

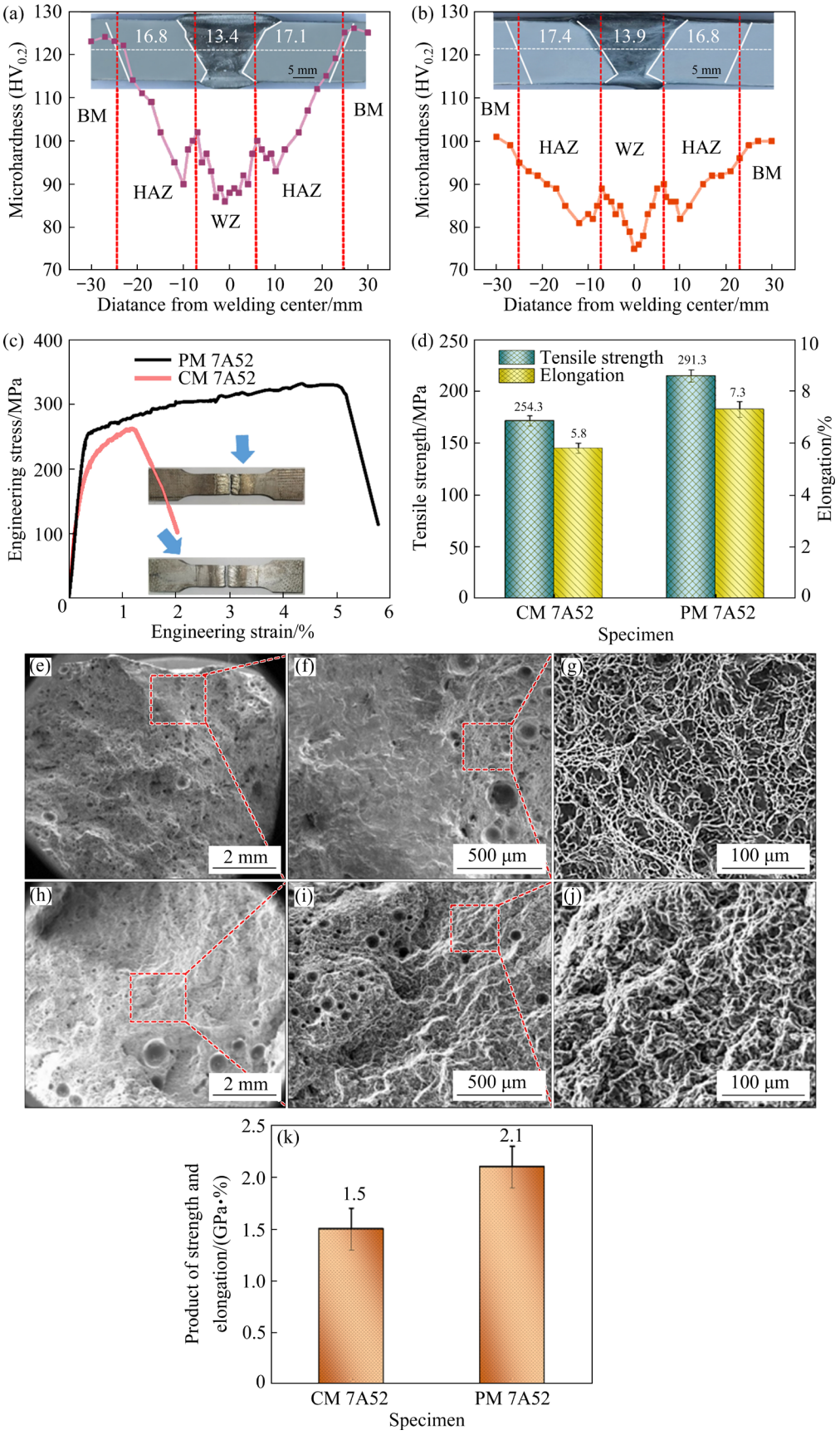

Fig. 10 Microhardness distribution curves of PM 7A52 (a) and CM 7A52 (b); Engineering stress−strain curves (c) and histogram of tensile strength and elongation (d); Tensile fracture morphologies of PM 7A52 (e−g) and CM 7A52 (h−j); Histogram of product of strength and elongation (k)

4 Discussion

4.1 Improvement of microstructure of welded joint

Welding microstructure plays a crucial role in determining the welding performance. Figure 12 illustrates the microstructure near the fusion line for PM 7A52 and CM 7A52 aluminum alloys. Due to the high cooling rate and temperature gradient during welding, epitaxial solidification occurred in the fusion zone (FZ), with grains growing perpendicularly to the BM grains and attaching to the semi-fused grains in the HAZ. Compared to CM 7A52, PM 7A52 exhibited a wider weld width (Figs. 10(a) and (b)) and a narrower fusion line (Figs. 12(a) and (e)), which contributed to the improved weld performance. Grain refinement near the FZ of PM 7A52 was attributed to the dispersed nanoparticles, which inhibited grain boundary migration under the heat input, limiting grain growth in HAZ. Consequently, PM 7A52 exhibited reduced texture and smaller grain gradients from the FZ to the BM, enhancing its weld microstructure.

As shown in Figs. 12(b) and (f), the proportion of small-angle grain boundaries in the WZ, FZ, and HAZ of PM 7A52 exhibited minimal variation. In contrast, CM 7A52 showed a significantly lower number of small-angle grain boundaries in the FZ and WZ compared to the HAZ. This microstructural inhomogeneity, driven by variations in small-angle grain boundaries, can significantly impact the mechanical properties. A comparison of Figs. 12(c) and (g) revealed that CM 7A52, which exhibited a higher Schmid factor across the WZ, FZ, HAZ, and BM, had an increased susceptibility to cracking. Additionally, the dislocation density in PM 7A52 was relatively low and uniformly distributed throughout the WZ, FZ, HAZ, and BM, as shown in Figs. 12(d) and (h). In contrast, CM 7A52 tended to

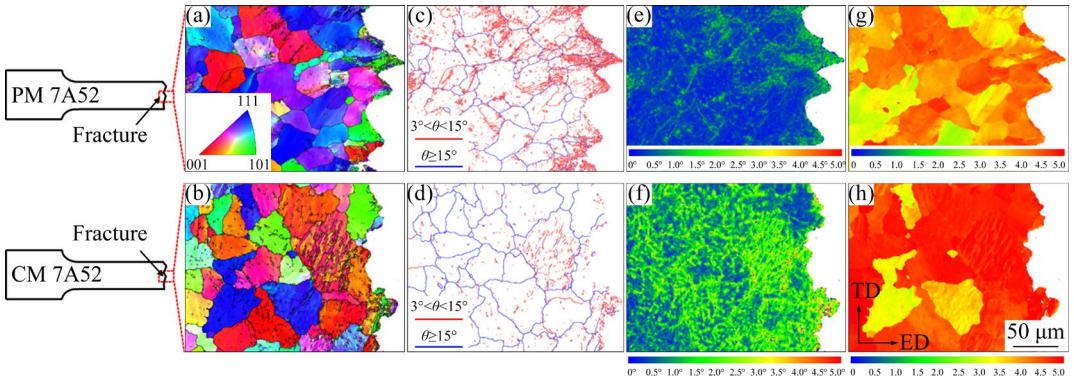

Fig. 11 Grain orientation distribution near fracture in PM 7A52 (a) and CM 7A52 (b); Distribution of grain boundaries in PM 7A52 (c) and CM 7A52 (d); Distribution of local misorientation in PM 7A52 (e) and CM 7A52 (f); Schmid factor distribution in PM 7A52 (g) and CM 7A52 (h)

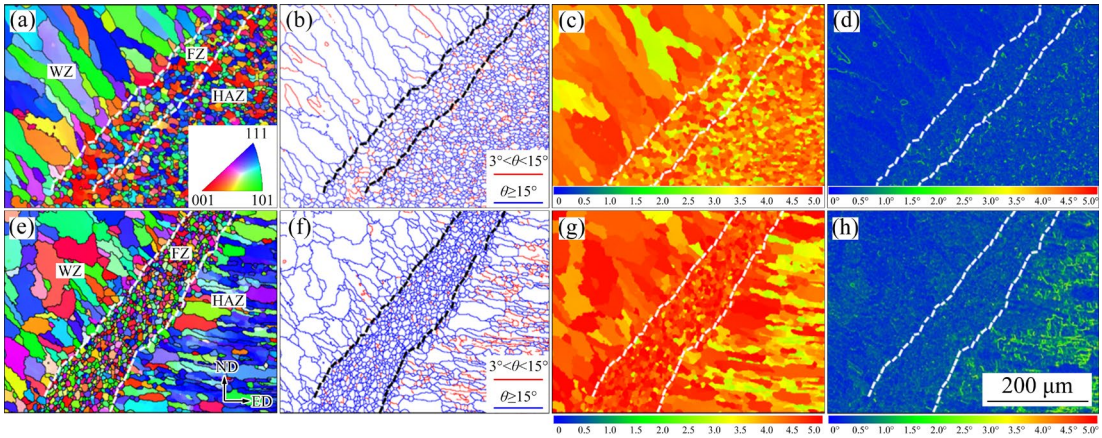

Fig. 12 Distribution of grain orientation near FZ in PM 7A52 (a) and CM 7A52 (e); Distribution of grain boundary in PM 7A52 (b) and CM 7A52 (f); Distribution of Schmid factor of PM 7A52 (c) and CM 7A52 (g); Distribution of local misorientation of PM 7A52 (d) and CM 7A52 (h)

develop localized dislocation concentrations, particularly in the WZ and HAZ, increasing the risk of stress concentration and cracking [52,53].

4.2 Reduction of residual stress in welded joint

The reduction in residual stress in the WZ of PM 7A52 was primarily attributed to the grain size and dislocation density. As shown in Figs. 5(a) and (g), the average grain size of PM 7A52 was smaller, likely due to the presence of Al_2O_3 particles in the BM, which entered the WZ during welding. These particles, with their excellent thermal stability, inhibited the grain growth [33]. While grain refinement can sometimes lead to the increased stress, Figs. 13(a)−(d) illustrate the morphology and FTT-filtered images of PM 7A52 and CM 7A52 in the WZ, revealing average lattice spacings of 0.2091 and 0.2155 nm, respectively. Given the known tensile stress in the WZ (Figs. 9(c) and (f)), higher lattice spacing is typically associated with larger residual stress. Figures 13(e)−(h) present the dislocation distribution in the WZ for both alloys. The dislocation lines in CM 7A52 were highly entangled, whereas PM 7A52 exhibited fewer dislocation lines, resulting in a lower dislocation density (see Figs. 7(a) and (g)). The higher dislocation density in CM 7A52 caused significant lattice distortion, thereby elevating residual stress. In contrast, the reduced dislocation density in PM 7A52 accounted for its lower residual stresses in the WZ. Figures 13(i)−(l) show GPA analysis results of PM 7A52 and CM 7A52 based on Figs. 13(b) and (d). The analysis indicates that the presence of Al_2O_3 particles reduced the lattice distortion, as evidenced by the lower ε_{xx} and ε_{yy} values, leading to diminished microstress and, consequently, lower residual stress in PM 7A52.

4.3 Improvement of welded joint strength

By comparing the weld microstructure and mechanical properties of PM 7A52 and CM 7A52 aluminum alloys, it was discovered that the enhanced strength of PM 7A52 welded joints primarily originated from the multifaceted strengthening mechanisms, including dispersion strengthening and grain boundary strengthening. According to the strengthening mechanisms of conventional aluminum alloys [54] and powder metallurgy Al−Zn−Mg−Cu alloys [45], the strength of welded joints of aluminum alloys ($\sigma_{strength}$) can be expressed

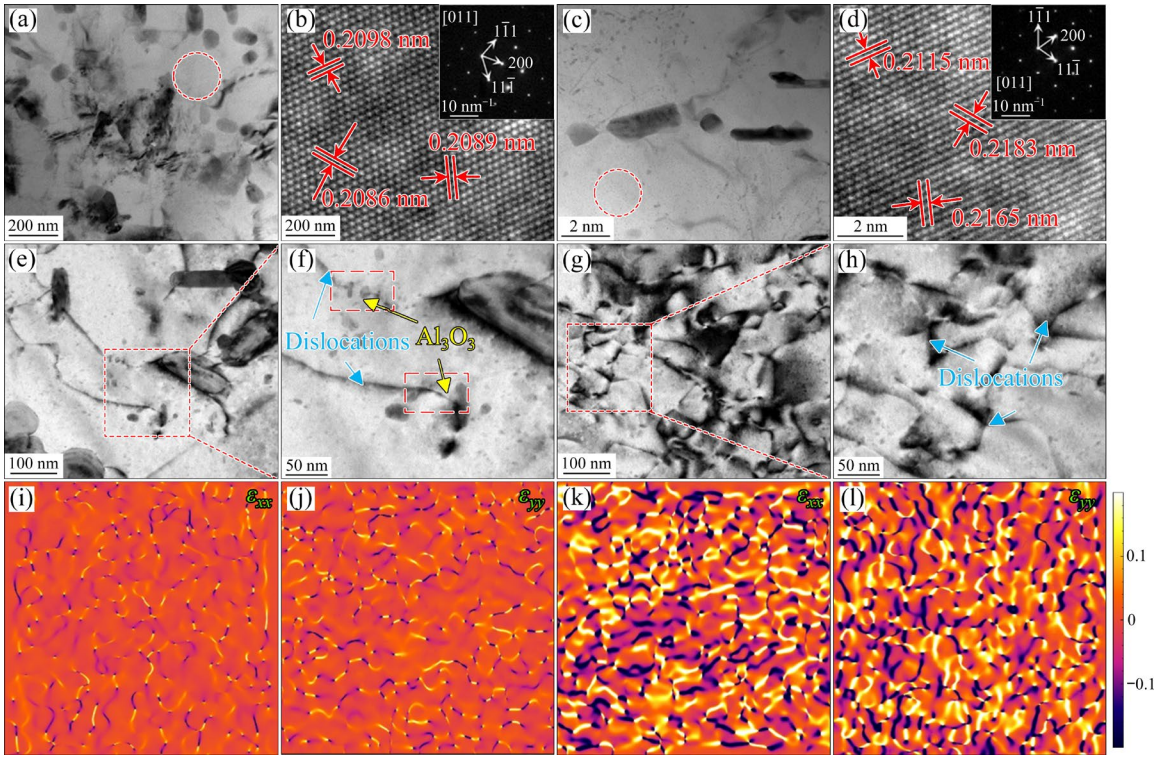

Fig. 13 Morphology and FTT-filtered images in WZ of PM 7A52 (a, b) and CM 7A52 (c, d); Dislocation distribution in WZ of PM 7A52 (e, f) and CM 7A52 (g, h); GPA analysis results of ε_{xx} and ε_{yy} distribution for (b) in PM 7A52 (i, j) and (d) in CM 7A52 (k, l)

as the sum of the following strengthening contributions

$$\sigma_{strength}=\sigma_{Al}+\Delta\sigma_{gb}+\Delta\sigma_{d}+\Delta\sigma_{ss}+\Delta\sigma_{ppt}+\Delta\sigma_{alumina} \quad (6)$$

where σ_{Al} is the yield strength of pure aluminum, 45 MPa [55], $\Delta\sigma_{gb}$, $\Delta\sigma_{d}$, $\Delta\sigma_{ss}$, $\Delta\sigma_{ppt}$ and $\Delta\sigma_{alumina}$ represent the strength increments contributed by grain boundaries, dislocations, solid-solution, precipitates and γ-Al_2O_3, respectively. Under T6 heat treatment conditions, a significant number of atoms form secondary phases, reducing the number of atoms in the solid solution. Consequently, the contribution of solid-solution strengthening to the total strength becomes negligible [56]. Furthermore, the primary phase in the WZ of PM 7A52 and CM 7A52 is the $MgZn_2$ phase (as shown in Fig. 14). From Figs. 3(c3) and (d3), and Fig. 4(b), it can be observed that there is minimal difference in the number and size of precipitate phases (e.g., $MgZn_2$, Mg_2Si) in the WZ of both alloys. Thus, the impact of precipitation strengthening on the difference in joint strength between PM 7A52 and CM 7A52 is considered negligible. Thus, the strength increment ($\Delta\sigma_{strength}$) can be expressed by

$$\Delta\sigma_{strength}=\Delta\sigma_{gb}+\Delta\sigma_{d}+\Delta\sigma_{alumina} \quad (7)$$

The effect of grain boundary strengthening was enhanced in the WZ of PM 7A52 due to the relatively high number of small-angle grain boundaries (as shown in Figs. 6(a) and (g)). The grain boundary strengthening $\Delta\sigma_{gb}$ is calculated from the Hall−Petch formula [57,58]:

$$\Delta\sigma_{gb}=kd^{-1/2} \quad (8)$$

where d is the average grain size in the WZ, and k is a material constant, for Al−Zn−Mg−Cu alloy it is 0.12 MPa·m$^{-1/2}$. The average grain sizes in the WZ of the PM 7A52 and CM 7A52 were 28.9 and 36.7 μm, respectively. Based on these values, the strength increments due to grain boundary strengthening for PM 7A52 and CM 7A52 were 22.3 and 19.8 MPa, respectively.

According to Table 4, the dislocation density in the WZ of PM 7A52 was lower than that of CM 7A52. The dislocation strengthening $\Delta\sigma_{d}$ can be calculated using the Bailey−Hirsch formula [59]:

$$\Delta\sigma_{d}=M\alpha Gb\rho^{1/2} \quad (9)$$

where M is the average orientation factor for FCC metal (3.06), α is a constant (0.2 for the FCC metal), G is the shear modulus (26.9 GPa for aluminum alloy), and ρ is the dislocation density of the GNDs,

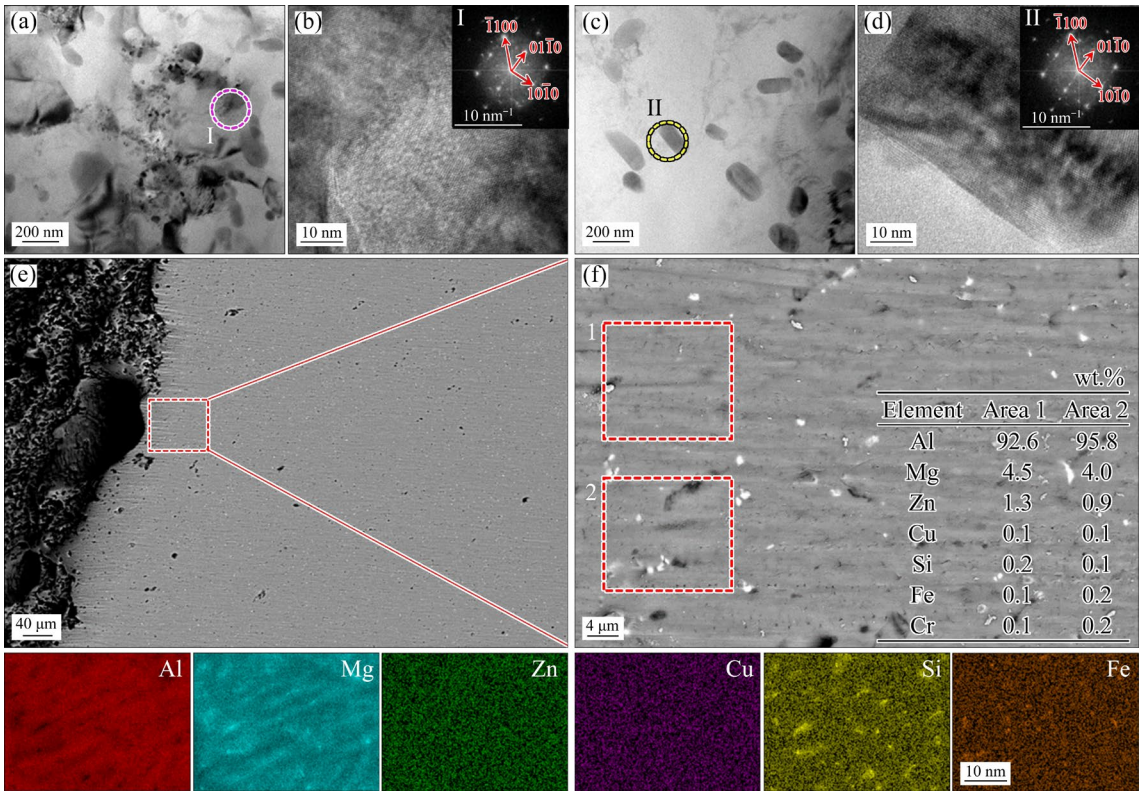

Fig. 14 Phase morphologies of WZ in PM 7A52 (a, b) and CM 7A52 (c, d); Morphology and EDS elemental scanning results of PM 7A52 near tensile fracture (e, f)

as listed in Table 4. The strength increments due to dislocation strengthening for PM 7A52 and CM 7A52 were calculated to be 64.8 and 66.9 MPa, respectively. Combining the contributions of grain boundary strengthening and dislocation strengthening, the total strength increments for PM 7A52 and CM 7A52 were 87.1 and 86.7 MPa, respectively.

The morphology and EDS results near the tensile fracture of PM 7A52 and CM 7A52 are shown in Fig. 14. It was observed that the content of Zn and Cr near the fracture deviated from the standard ER 5356 composition, with Zn being higher and Cr being lower. This variation likely occurred because portions of PM 7A52 entered the weld seam in a molten state and solidified during welding. Consequently, it can be inferred that the WZ contained Al_2O_3 particles.

To investigate the presence of Al_2O_3 particles in the WZ, the morphology, high-resolution diffraction rings, and face-scan EDS distributions of the BM and WZ in PM 7A52 aluminum alloy were analyzed. TEM measurements of the WZ and BM were conducted in the central layer of the plate, with the WZ observation positioned at the center along the ED. As shown in Figs. 15(a)−(d), a comparison of the polycrystalline diffraction rings with the PDF#75-0921 standard card confirmed that the black particles were γ-Al_2O_3 particles, ranging in size from 5 to 50 nm [45]. Further comparison of the distribution of γ-Al_2O_3 particles in the BM and WZ (Figs. 15(e)−(h) and 15(i)−(l)) revealed that these particles were uniformly dispersed in both regions. Notably, a higher concentration of γ-Al_2O_3 particles was observed in the BM compared to the WZ, primarily due to the incorporation of γ-Al_2O_3 particles from the BM into the WZ. The dispersion of γ-Al_2O_3 particles significantly enhanced the tensile strength and microhardness of the weld in powder metallurgy aluminum alloys, contributing to an improvement in mechanical properties through dispersion strengthening [60,61]. To quantify the strength enhancement induced by γ-Al_2O_3 particle dispersion in PM 7A52, the following equations were used for calculation:

$$\Delta\sigma_{\text{alumina}}=MGb\cdot\ln[\pi r/(2b)]/(2\pi\lambda_1\sqrt{1-v}) \quad (10)$$

$$\lambda_1=2r\left[\sqrt{\pi/(3\sqrt{3}f_v)}-\pi/4\right] \quad (11)$$

where v is Poisson's ratio (0.33 for aluminum alloys), r is the average radius of the phase, λ_1 is the inter-edge phase spacing, and f_v is the volume fraction of the precipitates. The values of r and f_v are listed in Table 5. The calculated results indicated

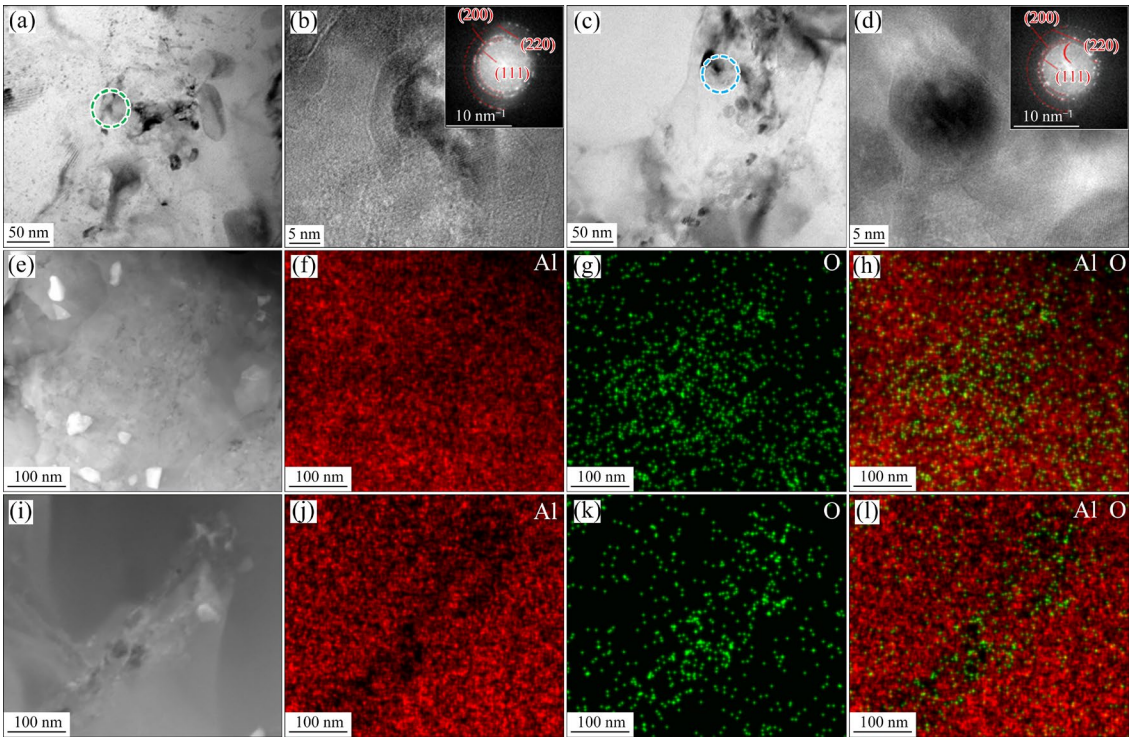

Fig. 15 Morphologies of γ-Al_2O_3, high-resolution images, and diffraction rings in BM (a, b) and WZ (c, d) of PM 7A52; Face-scan EDS results of γ-Al_2O_3 in BM (e−h) and WZ (i−l) of PM 7A52

Table 5 Microstructural characteristics of γ-Al_2O_3 particles in WZ of PM 7A52

r/nm	f_v/%
28	0.46

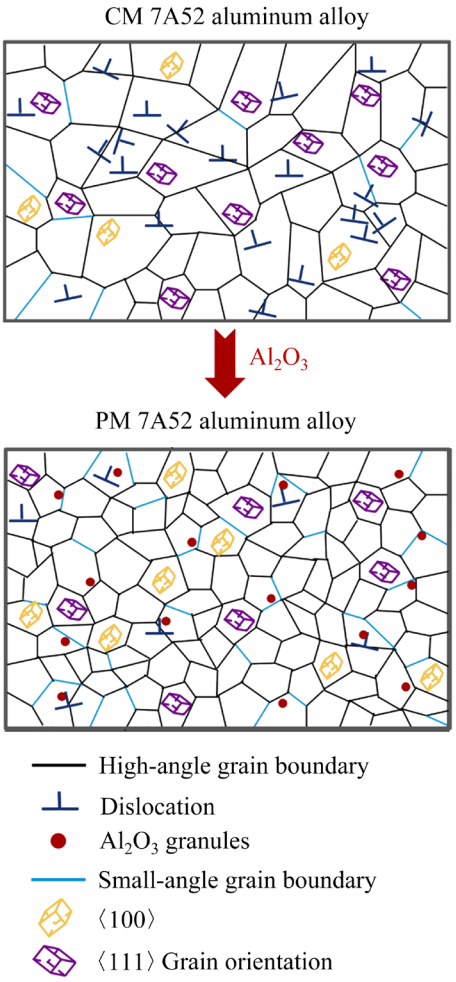

Fig. 16 Mechanism of γ-Al_2O_3 particles in weld of PM 7A52

that the strength contribution from dispersion strengthening in the WZ of PM 7A52 was 52.1 MPa. In summary, the total strength increment of PM 7A52 compared to CM 7A52 in the WZ was 52.5 MPa, considering the combined effects of dispersion strengthening, grain boundary strengthening, and dislocation strengthening. Since the effects of γ-Al_2O_3 dispersion strengthening and grain boundary strengthening are not linearly additive, the actual strength was typically lower than the calculated value. Overall, PM 7A52 significantly improved the weld microstructure, reduced weld residual stress, and enhanced mechanical properties such as microhardness and tensile strength. The mechanism, by which Al_2O_3 particles influence the WZ of PM 7A52, is illustrated in Fig. 16. Future work will involve replacing the ER 5356 welding wire with powder metallurgy welding wire to further enhance the mechanical properties of welded joints while maintaining low residual stress levels.

5 Conclusions

(1) In-situ generated nano-Al_2O_3 dispersion strengthening PM 7A52 and CM 7A52 aluminum alloys were MIG welded. The grain size in the WZ, HAZ, and BM of PM 7A52 was refined to varying degrees after welding. Additionally, the number of small-angle grain boundaries in the WZ of PM 7A52 increased by 5.3% compared to that of CM 7A52.

(2) PM 7A52 aluminum alloy effectively reduced dislocation density in the WZ, HAZ, and BM, lowering the risk of stress concentration. It also reduced texture strength, with pole density values in the WZ of PM 7A52 (3.6) being lower than those of CM 7A52 (5.6).

(3) Internal residual stress analysis performed with self-developed SWXRD equipment revealed that the residual stress in the WZ of PM 7A52 was about 38 MPa lower than that of CM 7A52.

(4) In the WZ, the average microhardness of PM 7A52 (HV 88) was about 17% higher than that of CM 7A52 (HV 75). Furthermore, the tensile strength and elongation of the welded joints of PM 7A52 were approximately 15% and 26% higher, respectively, compared to those of CM 7A52. The enhanced tensile strength in the welded joints of PM 7A52 was primarily attributed to the grain boundary strengthening and the dispersion strengthening caused by γ-Al_2O_3 particles.

CRediT authorship contribution statement

Jing-han YANG: Conceptualization, Methodology, Investigation, Data curation, Formal analysis, Visualization, Writing − Original draft; **Peng-fei JI** and **Lin-yang WU:** Methodology, Investigation; **Xiao-yun DING:** Data curation; **Jin-chao JIAO:** Investigation; **Meng-hui CUI:** Formal analysis; **Xing-yu CHEN:** Methodology; **Jin ZHANG:** Conceptualization, Resources, Writing − Review & editing, Funding acquisition, Project administration; **Yong LIAN:** Methodology, Investigation; **Lin ZHENG:** Conceptualization, Resources, Writing − Review & editing; **Shi-tao DOU:** Formal analysis.

Declaration of competing interest

The authors declare that they have no known competing financial interests or personal relationships that could have appeared to influence the work reported in this paper.

Acknowledgments

This work was supported by the National Key Research and Development Program of China (No. SQ2021YFF0600011).

References

[1] WANG Dang, ZHANG Wen-xue, YI You-ping, HUANG Shi-quan, HE Hai-lin, ZHANG Jing-jing. Influence of retrogression temperature and time on microstructure, mechanical properties and corrosion behaviors of cryogenically-deformed 7A85 aluminum alloy [J]. Transactions of Nonferrous Metals Society of China, 2024, 34(2): 392−407.

[2] YANG Xian-wen, YE Ling-ying, ZHANG Yong, CHENG Quan-shi. Effect of interrupted aging on mechanical properties and corrosion resistance of 7A75 aluminum alloy [J]. Transactions of Nonferrous Metals Society of China, 2024, 34(8): 2415−2430.

[3] SUN Yi, YI Zhong-huai, SHEN Ting, XIONG Hui-wen, KANG Xiao, ZHANG Lei, ZHOU Ke-chao. Microstructure and mechanical properties of 7075 aluminum alloy prepared by metal fused deposition modeling [J]. Transactions of Nonferrous Metals Society of China, 2024, 34(7): 2108−2119.

[4] FENG Yue-hai, CHEN Jia-he, QIANG Wei, WANG Ke-hong. Microstructure and mechanical properties of aluminium alloy 7A52 thick plates welded by robotic double-sided coaxial GTAW process [J]. Materials Science and Engineering: A, 2016, 673: 8−15.

[5] HUANG Ji-wu, YIN Zhi-min, LEI Xue-feng. Microstructure and properties of 7A52 Al alloy welded joint [J]. Transactions of Nonferrous Metals Society of China, 2008, 18(4): 804−808.

[6] KHOSHROYAN A, DARVAZI A R. Effects of welding parameters and welding sequence on residual stress and distortion in Al6061-T6 aluminum alloy for T-shaped welded joint [J]. Transactions of Nonferrous Metals Society of China, 2020, 30(1): 76−89.

[7] XUE Jun-yu, LI Yuan-xing, CHEN Hui, ZHU Zong-tao. Wettability, microstructure and properties of 6061 aluminum alloy/304 stainless steel butt joint achieved by laser-metal inert-gas hybrid welding-brazing [J]. Transactions of Nonferrous Metals Society of China, 2018, 28(10): 1938−1946.

[8] IMAM FAUZI E R, CHE JAMIL M S, SAMAD Z, MUANGJUNBUREE P. Microstructure analysis and mechanical characteristics of tungsten inert gas and metal inert gas welded AA6082-T6 tubular joint: A comparative study [J]. Transactions of Nonferrous Metals Society of China, 2017, 27(1): 17−24.

[9] YI Jie, ZHANG Jian-ming, CAO Shu-fen, GUO Peng-cheng. Effect of welding sequence on residual stress and deformation of 6061-T6 aluminium alloy automobile component [J]. Transactions of Nonferrous Metals Society of China, 2019, 29(2): 287−295.

[10] HE Peng, WU Yun-xin, ZHANG Tao, CHEN Song-yi, ZHANG Chen. Residual stresses in linear friction welding of TC17 titanium alloy considering phase fraction [J]. Transactions of Nonferrous Metals Society of China, 2024, 34(1): 184−193.

[11] HU Zhi, RUAN Xian-ming, YAN Hong. Effects of neodymium addition on microstructure and mechanical properties of near-eutectic Al−12Si alloys [J]. Transactions of Nonferrous Metals Society of China, 2015, 25(12): 3877−3885.

[12] WANG Yu, DENG Yun-lai, DAI Qing-song, JIANG Ke-da, CHEN Ji-qiang, GUO Xiao-bin. Microstructures and strengthening mechanisms of high Fe containing Al−Mg−Si−Mn−Fe alloys with Mg, Si and Mn modified [J]. Materials Science and Engineering: A, 2021, 803: 140477.

[13] JIA Zhi-hong, ZHOU Guang-wen, ZHOU Hong-yu, LIU Fei, DING Li-peng, WENG Yao-yao, XIANG Kai-yun, ZHAO Hai-dong. Effects of Cu content and heat treatment process on microstructures and mechanical properties of Al−Si−Mg−Mn−*x*Cu cast aluminum alloys [J]. Transactions of Nonferrous Metals Society of China, 2024, 34(3): 737−754.

[14] MAJCHROWICZ K, PAKIEŁA Z, CHROMINSKI W, KULCZYK M. Enhanced strength and electrical conductivity of ultrafine-grained Al−Mg−Si alloy processed by hydrostatic extrusion[J]. Materials Characterization, 2018, 135: 104−114.

[15] LIU C H, CHEN J, LAI Y X, ZHU D H, GU Y, CHEN J H. Enhancing electrical conductivity and strength in Al alloys by modification of conventional thermo-mechanical process [J]. Materials & Design, 2015, 87: 1−5.

[16] KRYMSKIY S, SITDIKOV O, AVTOKRATOVA E, MARKUSHEV M. 2024 aluminum alloy ultrahigh-strength sheet due to two-level nanostructuring under cryorolling and heat treatment [J]. Transactions of Nonferrous Metals Society of China, 2020, 30(1): 14−26.

[17] PAN De-cong, PAN Qing-lin, YU Qing-bin, LI Guo-liang, LIU Bing, DENG Ying, LIU Hua. Microstructure and fatigue behavior of MIG-welded joints of 6005A aluminum alloy with trace amounts of scandium [J]. Materials Characterization, 2022, 194: 112482.

[18] WANG Bo, XUE Song-bai, MA Chao-li, HAN Yi-long, LIN Zhong-qiang. Effect of combinative addition of Ti and Sr on modification of AA4043 welding wire and mechanical properties of AA6082 welded by TIG welding [J]. Transactions of Nonferrous Metals Society of China, 2017, 27(2): 272−281.

[19] DONG Ming-ye, ZHAO Yue, LI Quan, WANG Fu-de, WU Ai-ping. Effects of Cd addition in welding wires on microstructure and mechanical property of wire and arc additively manufactured Al−Cu alloy [J]. Transactions of Nonferrous Metals Society of China, 2022, 32(3): 750−764.

[20] YAN Shao-hua, XING Bo-bin, ZHOU Hai-yang, XIAO Yi, QIN Qing-Hua, CHEN Hui. Effect of filling materials on the microstructure and properties of hybrid laser welded Al−Mg−Si alloys joints [J]. Materials Characterization, 2018, 144: 205−218.

[21] ZHONG Shi-biao, HAN Shuang, CHEN Ji-qiang, REN Jie-ke, ZHOU Zi-xiang, WEN Feng, QI Liang, GUAN Ren-guo. Microstructure and properties of 7075 aluminum alloy welding joint using different filler metals [J]. Materials Today Communications, 2022, 31: 103260.

[22] HU Wei, LI Qing-hua, WANG Yue, BAI Wei, LIANG Zhi-min, YAN De-jun. Effect of welding parameters on

microstructure and mechanical properties of friction-stir-welded Al−Mg−Si alloy [J]. Journal of Materials Engineering and Performance, 2020, 29(2): 866−876.

[23] CAO Xue-long, WANG Gang, XING Chang, TAN Cai-wang, JIANG Jun-jun. Effect of process parameters on microstructure and properties of laser welded joints of aluminum/steel with Ni/Cu interlayer [J]. Transactions of Nonferrous Metals Society of China, 2021, 31(8): 2277−2286.

[24] CORNACCHIA G, CECCHEL S, PANVINI A. A comparative study of mechanical properties of metal inert gas (MIG)-cold metal transfer (CMT) and fiber laser-MIG hybrid welds for 6005A T6 extruded sheet [J]. The International Journal of Advanced Manufacturing Technology, 2018, 94(5): 2017−2030.

[25] TEYEB A, SILVA J, KANFOUD J, CARR P, GAN T H, BALACHANDRAN W. Improvements in the microstructure and mechanical properties of aluminium alloys using ultrasonic-assisted laser welding [J]. Metals, 2022, 12(6): 1041.

[26] CHENG Xian-ming, YANG Ke, LIU Si-zhan, JI Shan-lin, WANG Jian. Microstructure and mechanical properties of ultrasonic welded copper to aluminum cables joints [J]. Transactions of Nonferrous Metals Society of China, 2023, 33(10): 3027−3038.

[27] WANG Zhang-wei, SONG Min, SUN Chao, HE Yue-hui. Effects of particle size and distribution on the mechanical properties of SiC reinforced Al−Cu alloy composites [J]. Materials Science and Engineering: A, 2011, 528(3): 1131−1137.

[28] TOPCU I, GULSOY H O, KADIOGLU N, GULLUOGLU A N. Processing and mechanical properties of B_4C reinforced Al matrix composites [J]. Journal of Alloys and Compounds, 2009, 482(1): 516−521.

[29] YE Xiang-ping, LI Ying-lei, WENG Ji-dong, CAI Ling-cang, LIU Cang-li. Research status on strengthening mechanism of particle-reinforced metal matrix composites [J]. Journal of Materials Engineering, 2018, 46(12): 28−37. (in Chinese)

[30] MEHRABI K, KHODABAKHSHI F, ZAREH E, SHAHBAZKHAN A, SIMCHI A. Effect of alumina nanoparticles on the microstructure and mechanical durability of meltspun lead-free solders based on tin alloys [J]. Journal of Alloys and Compounds, 2016, 688: 143−155.

[31] WENG Fei, CHRN Chuan-zhong, YU Hui-jun. Research status of laser cladding on titanium and its alloys: A review [J]. Materials & Design, 2014, 58: 412−425.

[32] WANG Tao, HUANG Yu-feng, YANG Lun, MA Yun-zhu, LIU Chao, WU Lei, YAN Huan-yuan, ZHAO Xin-yue, LIU Wen-sheng. Microstructure and mechanical properties of 7055 Al alloy prepared under different sintering conditions using powder by-products [J]. Materials Science and Engineering: A, 2021, 805: 140562.

[33] CHEN Cun-guang, LI Feng, HAN Wei-hao, LU Tian-xing, LI Pei, CUI Qian-yue, SUI Yan-li, GUO Zhi-meng, VOLINSKY A A. Thermally stable Al conductor prepared from Al powder with a low oxygen content [J]. Materials Science and Engineering: A, 2021, 813: 141174.

[34] SOKOLUK M, CAO Che-zheng, PAN Shuai-hang, LI Xiao-chun. Nanoparticle-enabled phase control for arc welding of unweldable aluminum alloy 7075 [J]. Nature Communications, 2019, 10(1): 98.

[35] MA Chao, CHEN Lian-yi, CAO Che-zheng, LI Xiao-chun. Nanoparticle-induced unusual melting and solidification behaviours of metals [J]. Nature Communications, 2017, 8(1): 14178.

[36] SABRY N, STROH J, SEDIAKO D. Characterization of microstructure and residual stress following the friction stir welding of dissimilar aluminum alloys [J]. CIRP Journal of Manufacturing Science and Technology, 2023, 41: 365−379.

[37] JAMES M N, HUGHES D J, HATTINGH D G, MILLS G, WEBSTER P J. Residual stress and strain in MIG butt welds in 5083-H321 aluminium: As-welded and fatigue cycled [J]. International Journal of Fatigue, 2009, 31(1): 28−40.

[38] GUO Jiang, FU Hai-yang, PAN Bo, KANG Ren-ke. Recent progress of residual stress measurement methods: A review [J]. Chinese Journal of Aeronautics, 2021, 34(2): 54−78.

[39] GUO Shun, ZHANG Hui-hui, KWAK Min-kyung, DING Wang, LIU Guang-lei, MA Wen, LIU Hai-xia, MENG Qing-kun, ZHAO Xin-qing. In-situ synchrotron X-ray diffraction investigation on deformation behavior of Nb/NiTi composite during pre-straining process [J]. Transactions of Nonferrous Metals Society of China, 2022, 32(8): 2609−2619.

[40] JI Peng-fei, ZHANG Jin, ZHENG Lin, XIAO Yong, DOU Shi-tao, CUI Xiao-ming, LIAN Yong. Comparison of residual stress determination using different crystal planes by short-wavelength X-ray diffraction in a friction-stir-welded aluminum alloy plate [J]. Journal of Materials Science, 2017, 52(21): 12834−12847.

[41] JI Peng-fei, YANG Zhong-yu, ZHANG Jin, ZHENG Lin, JI V, KLOSEK V. Residual stress distribution and microstructure in the friction stir weld of 7075 aluminum alloy [J]. Journal of Materials Science, 2015, 50(22): 7262−7270.

[42] WOO W, AN G B, TRUMAN C E, JIANG W C, HILL M R. Two-dimensional mapping of residual stresses in a thick dissimilar weld using contour method, deep hole drilling, and neutron diffraction [J]. Journal of Materials Science, 2016, 51(23): 10620−10631.

[43] SHAMSUJJOHA M, AGNEW S R, FITZ-GERALD J M, MOORE W R, NEWMAN T A. High strength and ductility of additively manufactured 316L stainless steel explained [J]. Metallurgical and Materials Transactions A, 2018, 49(7): 3011−3027.

[44] ZHANG Cun-sheng, DONG Yuan-yuan, WANG Cui-xue, ZHAO Guo-qun, CHEN Liang, SUN Wen-chao. Evolution of transverse weld during porthole extrusion of AA7N01 hollow profile [J]. Journal of Materials Processing Technology, 2017, 248: 103−114.

[45] HAN Wei-hao, CHEN Cun-guang, LI Pei, LI Yang, SU Guo-ping, SUN Chun-fang, YANG Fang, VOLINSKY A A, GUO Zhi-meng. The conjoint influence of oxygen and hot extrusion on microstructure and mechanical properties of a powder metallurgy processed aluminum alloy [J]. Materials Science and Engineering: A, 2022, 861: 144317.

[46] YI Jie, WANG Guan, LI Shi-kang, LIU Zhi-wen, GONG Yan-li. Effect of post-weld heat treatment on microstructure and mechanical properties of welded joints of 6061-T6 aluminum alloy [J]. Transactions of Nonferrous Metals Society of China, 2019, 29(10): 2035−2046.

[47] REN Lei, XIAO Wen-long, KENT D, WAN Min, MA Chao-li, ZHOU Lian. Simultaneously enhanced strength and ductility in a metastable β-Ti alloy by stress-induced hierarchical twin structure [J]. Scripta Materialia, 2020, 184: 6−11.

[48] GUO Fu-qiang, DUAN Shu-wei, PAN Yu-zhe, WU Dong-ting, MATSUDA K, WANG Tao, ZOU Yong. Stress corrosion behavior and microstructure analysis of

Al−Zn−Mg−Cu alloys friction stir welded joints under different aging conditions [J]. Corrosion Science, 2023, 210: 110821.
[49] PAN Yu-zhe, WANG Yu, GUO Fu-qiang, ZHANG Tie-hao, MATSUDA K, WU Dong-ting, ZHANG Yong-ang, ZOU Yong. Stress corrosion behavior of friction stir welding joint of 7N01 aluminum alloy [J]. Journal of Materials Research and Technology, 2021, 15: 1130−1144.
[50] LIU Shuai-shuai, YANG Bang-peng, HUANG Guang-sheng, CHEN Xian-hua, TANG Ai-tao, JIANG Bin, ZHENG Kai-hong, PAN Fu-sheng. Effect of dual-heterogeneous microstructures on mechanical properties of AZ91 extruded sheet [J]. Transactions of Nonferrous Metals Society of China, 2023, 33(4): 1086−1097.
[51] YIN Dong-di, CHEN Bo, CHAI Yan-qin, WAN You-fu, ZHOU Hao, ZHENG Jiang, WANG Qu-dong, ZENG Ying. Statistical investigation of deformation mechanisms in rolled Mg sheet during compression [J]. Transactions of Nonferrous Metals Society of China, 2023, 33(10): 2970−2985.
[52] ZHANG Deng-kui, ZHAO Yue, DONG Ming-ye, WANG Guo-qing, WU Ai-ping, SHAN Ji-guo, MENG Dan-yang, LIU Xian-li, SONG Jian-ling, ZHANG Zhong-ping. Effects of weld penetration on tensile properties of 2219 aluminum alloy TIG-welded joints [J]. Transactions of Nonferrous Metals Society of China, 2019, 29(6): 1161−1168.
[53] ZHANG Wen-cong, LIU Yu-xuan, MA Jun-fei, WANG Wen-ke, CHEN Wen-zhen, LIU Xin-tong, YANG Jian-lei. Effects of bimodal basal texture on bending stress and microstructure evolution of Mg−2.6Nd−0.55Zn−0.5Zr alloys [J]. Transactions of Nonferrous Metals Society of China, 2023, 33(3): 714−727.
[54] BALOG M, KRIZIK P, BAJANA O, HU T, YANG H, SCHOENUNG J M, LAVERNIA E J. Influence of grain boundaries with dispersed nanoscale Al_2O_3 particles on the strength of Al for a wide range of homologous temperatures [J]. Journal of Alloys and Compounds, 2019, 772: 472−481.
[55] REN Jian, WANG Ri-chu, PENG Chao-qun, FENG Yan. Multistage aging treatment influenced precipitate characteristics improve mechanical and corrosion properties in powder hot-extruded 7055 Al alloy [J]. Materials Characterization, 2020, 170: 110683.
[56] MA K K, HU T, YANG H, TOPPING T, YOUSEFIANI A, LAVEINIA E J, SCHOENUNG J M. Coupling of dislocations and precipitates: Impact on the mechanical behavior of ultrafine grained Al−Zn−Mg alloys [J]. Acta Materialia, 2016, 103: 153−164.
[57] LEE S H, JUNG J G, BAIK S I, SEIDMAN D N, KIM M S, LEE Y K, EUH K. Precipitation strengthening in naturally aged Al−Zn−Mg−Cu alloy [J]. Materials Science and Engineering: A, 2021, 803: 140719.
[58] BAKHSHI R, FARSHIDI M H, SAJJADI S A. Strengthening of aluminium alloy 7005 through imposition of severe plastic deformation supplemented by different ageing treatments [J]. Transactions of Nonferrous Metals Society of China, 2021, 31(10): 2909−2921.
[59] ZHEREBTSOV S V, DYAKONOV G S, SALEM A A, SOKOLENKO V I, SALISHCHEV G A, SEMIATIN S L. Formation of nanostructures in commercial-purity titanium via cryorolling [J]. Acta Materialia, 2013, 61(4): 1167−1178.
[60] BALOG M, OROVCIK L, NAGY S, KRIZIK P, NOSKO M, OSLANEC P, ZIFCAK P. To what extent does friction-stir welding deteriorate the properties of powder metallurgy Al? [J]. Journal of Materials Research and Technology, 2020, 9(3): 6733−6744.
[61] TAO Xi-chen, CHANG Yong-qin, GUO Yuan-hang, LI Wu-ming, LI Ming-yang. Microstructure and mechanical properties of friction stir welded oxide dispersion strengthened AA6063 aluminum matrix composites enhanced by post-weld heat treatment [J]. Materials Science and Engineering: A, 2018, 725: 19−27.

粉末冶金 7A52 铝合金的 MIG 焊接组织、残余应力及力学性能

杨竞涵[1,2,3]，计鹏飞[4]，吴林阳[1,2,3]，丁啸云[1,2,3]，焦进超[1,2,3]，
崔梦辉[1,2,3]，陈星宇[1,2,3]，张 津[1,2,3]，连 勇[1,2,3]，郑 林[5]，窦世涛[1,5]

1. 北京科技大学 新材料技术研究院，北京 100083；
2. 北京科技大学 北京市腐蚀、磨蚀与表面技术重点实验室，北京 100083；
3. 北京科技大学 国家材料腐蚀与防护科学数据中心，北京 100083；
4. 北京科技大学 工程技术研究院，北京 100083；
5. 西南技术工程研究所，重庆 400039

摘 要：对原位生成纳米 Al_2O_3 的粉末冶金 7A52(PM 7A52)铝合金 MIG 焊进行研究。采用 EBSD 和 TEM 对显微组织进行分析。采用自主研发的 SWXRD 技术对宏观织构和内部残余应力进行分析。结果表明：PM 7A52 铝合金能有效降低焊后组织的晶粒尺寸、位错密度和织构强度。此外，与传统熔融铸 7A52 铝合金(CM 7A52)相比，PM 7A52 铝合金焊缝区(WZ)的残余应力降低了 38 MPa。特别地，PM 7A52 铝合金焊接接头的抗拉强度和伸长率分别提高了约 15%和 26%。接头抗拉强度的提高主要是由于晶界强化和 γ-Al_2O_3 颗粒进入 WZ 引起的弥散强化。

关键词：粉末冶金 7A52 铝合金；MIG 焊接；SWXRD 技术；织构；残余应力；力学性能

(Edited by Wei-ping CHEN)